UHT Metamorphism Peaking Above 1100 °C with Slow Cooling: Insights from Pelitic Granulites in the Jining Complex, North China Craton

Bin Wang[1], Chun-Jing Wei[1]*, Wei Tian[1] and Bin Fu[2]

[1]MOE Key Laboratory of Orogenic Belts and Crustal Evolution, School of Earth and Space Sciences, Peking University, Beijing 100871, China; [2]Research School of Earth Sciences, The Australian National University, Canberra, ACT 2601, Australia

*Corresponding author. Telephone: 86-10-62754157. Fax: 86-10-62751159. E-mail: cjwei@pku.edu.cn

ABSTRACT

The peak temperature and duration of ultrahigh-temperature (UHT) metamorphism are critical to identify and understand its tectonic environment. The UHT metamorphism of the Jining complex in the Khondalite Belt, North China Craton is controversial on the peak temperature, time and tectonic setting. A representative sapphirine-bearing granulite sample is selected from the classic Tianpishan outcrop for addressing the metamorphic evolution and timing. The rock is markedly heterogeneous on centimetre scale and can be divided into melanocratic domains rich in sillimanite (MD-s) or rich in orthopyroxene (MD-o), and leucocratic domains (LD). On the basis of detailed petrographic analyses and phase equilibria modelling using THERMOCALC, all three types of domains record peak temperatures of 1120–1140 °C and a series of post-peak cooling stages at 0·8–0·9 GPa to the fluid-absent solidus (∼890 °C), followed by sub-solidus decompression. The peak temperature for MD-s is constrained by the coexistence of sillimanite-I + sapphirine + spinel + quartz, where sillimanite-I contains densely exsolved aciculae of hematite, yielding reintegrated Fe_2O_3 contents up to 2·1–2·3 wt %. The post-peak cooling evolution involves the sequential appearance of K-feldspar, sillimanite-II + garnet, orthopyroxene and biotite, where sillimanite-II is exsolution-free and contains variable Fe_2O_3 contents of 1·3–1·8 wt %. The peak temperature for MD-o is constrained by the sapphirine + orthopyroxene assemblage, where orthopyroxene has a maximum Al^{IV} of 0·22 (Al_2O_3 = 9·5 wt %) in the core. The cooling evolution involves the sequential appearance of K-feldspar, garnet and biotite, and the decreasing Al^{IV} (0·22→0·17) from core to rim in orthopyroxene. The peak temperature for LD is constrained by the inferred K-feldspar-absent assemblage and the maximum anorthite content of 0·11 in K-feldspar. The cooling evolution involves the crystallization of segregated melts, exsolution of supra-solvus ternary feldspars and growth of biotite. The Al in orthopyroxene, Fe_2O_3 in sillimanite and anorthite in K-feldspar are good indicators for constraining extreme UHT conditions although they depend differently on bulk-rock compositions. In-situ SHRIMP U–Pb dating of metamorphic zircon indicates that the UHT metamorphism may have occurred at >1·94 Ga and the cooling under UHT conditions lasted over 40 Ma. The extreme UHT metamorphism in the Jining complex is interpreted to be triggered by the advective heating of intraplate hyperthermal mafic magmas together with a plume-related hot mantle upwelling, following an orogenic crustal thickening event.

Key words: Jining complex; pelitic granulite; slow cooling; temperature indicators; UHT metamorphism

INTRODUCTION

Ultrahigh-temperature (UHT) metamorphic crustal rocks are subjected to temperatures over 900 °C at only moderate pressure on regional scale (Ellis *et al.*, 1980; Harley, 1998*a*, 2008), which is difficult to explain with a normal tectonic scenario (e.g. Burg & Gerya, 2005; Kelsey, 2008; Sizova *et al.*, 2014). Continental back-arcs were widely favoured to generate UHT metamorphism with geothermal gradient of about 20–25 °C/km, due to their high heat flow (Collins, 2002; Hyndman *et al.*, 2005; Currie & Hyndman, 2006; Brown, 2006; Brown*et al.*, 2007). Numerical modelling indicated that a long-lived orogenic belt with extremely enriched internal heat-producing radioactive elements can autonomously attain UHT metamorphic conditions of 900–1000 °C (Clark *et al.*, 2011). Besides the above-mentioned processes, intra-continental rifting (e.g. Santosh & Omori, 2008; Tucker *et al.*, 2015; Zheng & Chen 2017), post-collision mantle upwelling (e.g. Platt *et al.*, 1998; Lee *et al.*, 2016) and mantle plume bombarding (e.g. Santosh *et al.*, 2008) were also proposed to influence the formation of UHT rocks. However, these tectonic regimes may not necessarily account for the extreme UHT metamorphism over 1100 °C with geothermal gradients exceeding 30 °C/km, such as those reported in the Napier Complex, Antarctica (Harley & Motoyoshi, 2000), the Central Highland complex, Sri Lanka (Sajeev & Osanai, 2004) and the Brasilia fold belt, Brazil (Moraes *et al.*, 2002). The genesis and tectonic attribution of such extreme UHT metamorphism are still not investigated to a sufficient depth.

Effective temperature indicators for UHT metamorphism are also urgently required. The traditional diagnostic mineral assemblages of UHT metamorphism such as sapphirine + quartz and orthopyroxene + sillimanite indicate wide temperatures ranging over 900–1000 °C (e.g. Harley, 2008; Kelsey, 2008). As Fe–Mg thermometry is mostly not applicable for quantifying UHT conditions considering the high efficiency of cationic diffusion (e.g. Kelsey & Hand, 2015), the Al in orthopyroxene thermometry has been employed as an available candidate to retrieve the temperatures of UHT metamorphism as the Al diffusion is much slower (e.g. Harley, 1998*b*; Harley & Motoyoshi, 2000; Hollis & Harley, 2003; Pattison *et al.*, 2003; Harley, 2004; Kelsey & Hand, 2015). For example, all the peak mineral assemblages in the UHT rocks from the aforementioned three localities have orthopyroxene, sapphirine and quartz with or without garnet and sillimanite, where orthopyroxene contains a maximum Al_2O_3 content over 12·5 wt % and records temperatures of 1120–1150 °C (Harley & Motoyoshi, 2000; Moraes *et al.*, 2002; Sajeev & Osanai, 2004). Nevertheless, the estimation of peak temperatures remains difficult in UHT rocks that do not contain orthopyroxene in the peak assemblage.

Most granulites, especially those peaking at UHT conditions, usually record prolonged slow cooling histories (e.g. Macdonald *et al.*, 2011; Wei *et al.*, 2014; Zhang *et al.*, 2015; Clark *et al.*, 2018; Laurent *et al.*, 2018), such as the UHT metamorphism in Rogaland, Norway (Laurent *et al.*, 2018) and the Napier complex, Antarctica (Clark *et al.*, 2018), which have cooling durations over 100 Ma under supra-solidus conditions. The UHT metamorphism with post-peak slow cooling (> 30 Ma) was interpreted to have formed at the hot underbelly of orogens with external heat source (e.g. Kelsey & Hand, 2015; Harley, 2016), which has been tested numerically by the protracted post-convergent ductile flow in orogenic cores (e.g. Jamieson & Beaumont, 2011). By contrast, the UHT metamorphism with post-peak fast cooling (mostly <10 Ma) is relatively limited, and is interpreted to be the result of severe lithospheric thinning and crustal extension accompanied by voluminous magmatism (e.g. Harley, 2016) or as lower pressure overprinting during rapid exhumation of deeply subducted continental slabs (e.g. Dong *et al.*, 2019). Thus, the duration of UHT metamorphism is also significant for understanding its geodynamic nature (e.g. Harley, 2016; Laurent *et al.*, 2018).

UHT metamorphism in the Jining complex, Khondalite Belt, North China Craton (NCC) (Fig. 1a, b) has attracted much attention and debates on both its peak temperature and metamorphic age in the last decade. For instance, the peak temperature of UHT granulites from the classic outcrops at Tuguishan and Tianpishan (Fig. 1c) is disputed to be 960–970 °C (Santosh *et al.*, 2009; Li & Wei, 2018), 1020–1050 °C (Jiao & Guo, 2011; Yang *et al.*, 2014) and >1100 °C (Liu *et al.*, 2011; Santosh *et al.*, 2012). As the peak temperature of UHT metamorphism is linked to its degree of anatexis, heat budget and tectonic environment, a robust and uncontested constraint on the temperature is required to understand the evolution of the terrane. Although a consensus seemed to have reached about the age of the UHT event at 1·91–1·92 Ga by zircon U–Pb dating (Santosh *et al.*, 2007*a*, 2013; Li & Wei, 2018; Lobjoie *et al.*, 2018; Li *et al.*, 2019), all of these ages are averaged from wide and continuous arrays usually from ~1·95 Ga to ~1·88 Ga on the concordia curve. A reliable and exact duration of the UHT metamorphism in the Jining complex is still unclear.

This study aims to determine the peak temperature and the duration of the UHT metamorphism at Tianpishan (Fig. 1c), using phase equilibria modelling and *in-situ* zircon dating approaches. We focus on a sapphirine-bearing pelitic granulite sample that is extremely heterogeneous and has different mineralogical or compositional domains. In particular, we evaluate the mineral compositions involving Al in orthopyroxene, Ca in K-feldspar and Fe^{3+} in sillimanite for their potential memories of UHT conditions.

GEOLOGIC SETTING

The Paleoproterozoic Khondalite Belt in the Western Block of the NCC extends in E–W direction for ~750 km. It is bordered by the Yinshan Block to the north and the
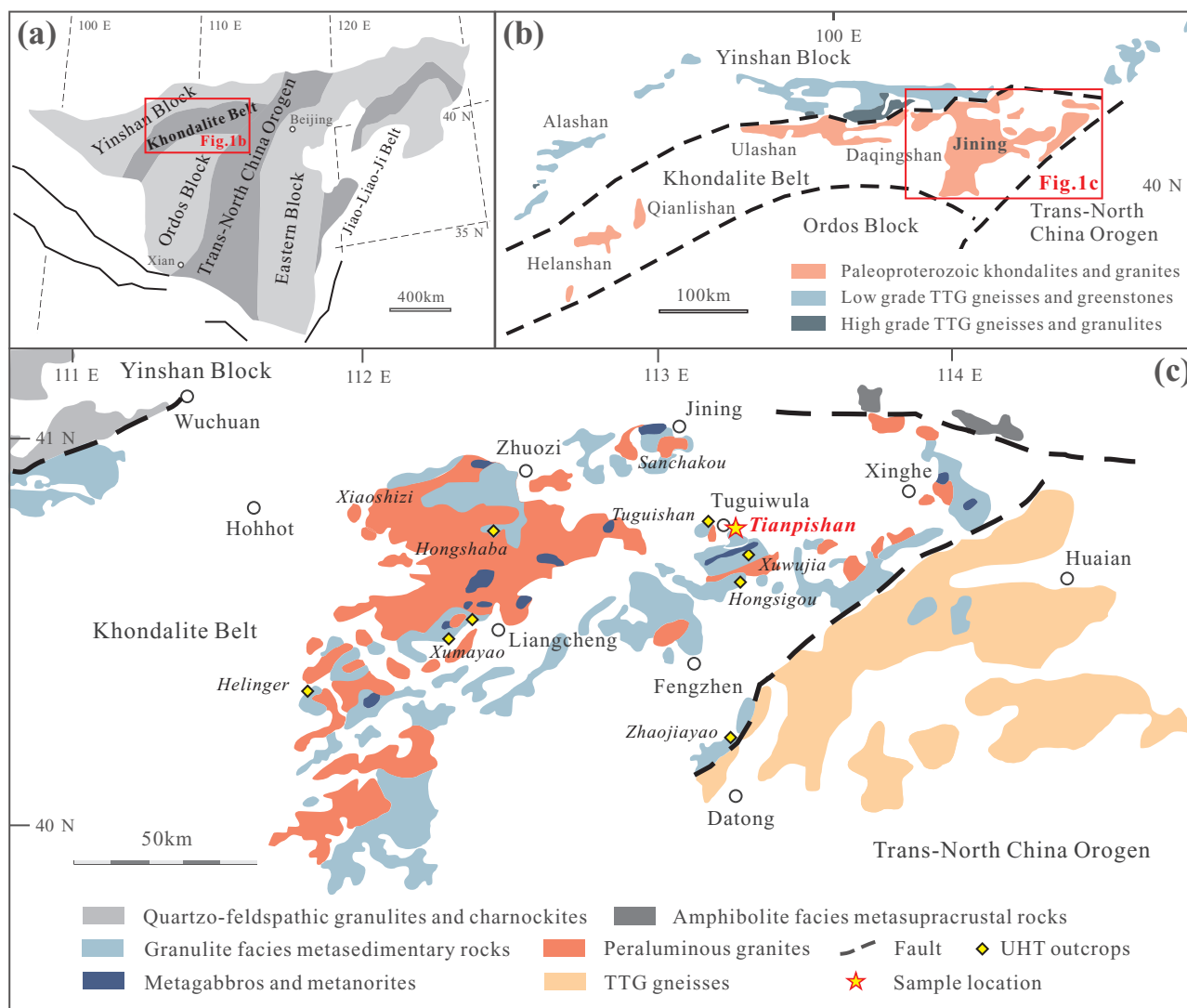
Fig. 1. (a) A tectonic sketch of the North China Craton (after Zhao *et al.*, 2005). (b) A geological map showing the distribution of the Khondalite Belt and adjacent tectonic units (after Zhao *et al.*, 2005). (c) A geological map showing the lithologic distribution in the Jining complex (modified after Guo *et al.*, 2001), with the sample locality of this study and the outcrops of UHT granulites from literature.

Ordos Block to the south (Fig. 1a, b), and is interpreted to have formed by a collision of these two blocks at ~1·95 Ga (e.g. Zhao *et al.*, 2005, 2012). The Khondalite Belt is intersected by the Paleoproterozoic Trans-North China Orogen along its eastern end.

The major rock types in the Khondalite Belt are high-grade metasediments (so called khondalite series), peraluminous granites, meta-mafic rocks and charnockites (e.g. Lu *et al.*, 1992; Zhao *et al.*, 1999; Guo *et al.*, 1999), which are exposed in the Helanshan–Qianlishan (west), Daqingshan–Ulashan (centre) and Jining (east) areas (Fig. 1b). The metasediments occur as high-pressure–normal–UHT granulite facies (e.g. Guo *et al.*, 2006; Zhou *et al.*, 2010; Cai *et al.*, 2014) roughly from west to east. The detrital zircon dates (2·3–2·0 Ga) from them give a depositional age younger than ~2·0 Ga, and the metamorphic zircon age suggests an intricate high-grade metamorphic history during 1·96–1·83 Ga (Wan *et al.*,

2006; Wu *et al.*, 2006; Santosh *et al.*, 2007*a*; Dong *et al.*, 2007, 2013; Yin *et al.*, 2009, 2011; Li *et al.*, 2011; Dan *et al.*, 2012; Cai *et al.*, 2015; Li & Wei, 2016, 2018). It has been suggested that the protoliths of these metasediments were deposited in cratonic basins (Condie *et al.*, 1992; Zhai & Peng, 2007), along passive continental margins (Lu *et al.*, 1996; Zhao *et al.*, 2005), or more probably, in back-arc extensional basins with their provenance being juvenile continental arc sediments of 2·2–2·0 Ga (Wan *et al.*, 2009; Dan *et al.*, 2012; Li & Wei, 2018). The peraluminous granites occur as minor leucogranitic veins with crystallization ages of 1·97–1·89 Ga (mean age = 1·94 Ga; Guo *et al.*, 1999), as well as massive garnet-bearing granite batholiths or intrusions with crystallization ages of 1·88–1·86 Ga in the Qianlishan–Helanshan area (Yin *et al.*, 2009, 2011) and 1·92–1·89 Ga in the Jining area (Guo *et al.*, 2002; Zhong *et al.*, 2007). They were possibly generated by the anatexis of the

metasediments (Shi *et al.*, 2018; Wang *et al.*, 2018). The mafic rocks mainly occur as gabbronorite with episodic crystallization ages of 2·45–2·10 Ga, 1·97–1·93 Ga and 1·85–1·84 Ga, and metamorphic ages of 1·95–1·83 Ga (Guo *et al.*, 1999; Peng *et al.*, 2010; Wan *et al.*, 2013; Liu *et al.*, 2014).

The Jining complex located at the eastern part of the Khondalite Belt comprises predominantly pelitic granulite/gneiss, peraluminous granite, and minor metagabbronorite (Fig. 1b, c). It has been studied intensively in the last decade owing to the increasing reports of UHT granulites, characterized by spinel- and sapphirine-bearing assemblages (e.g. Liu & Li, 2007; Santosh *et al.*, 2007b; Jiao & Guo, 2011; Zhang *et al.*, 2012; Liu *et al.*, 2012; Shimizu *et al.*, 2013; Yang *et al.*, 2014; Li & Wei, 2016, 2018; Lobjoie *et al.*, 2018; Li *et al.*, 2019). These UHT rocks have metamorphic ages of 1·91–1·92 Ga (Santosh *et al.*, 2007a; Li & Wei, 2018; Lobjoie *et al.*, 2018; Li *et al.*, 2019) and ∼1·88 Ga (Yang *et al.*, 2014). Their *P–T* paths were initially inferred as anticlockwise (Santosh *et al.*, 2009; Liu *et al.*, 2011; Shimizu *et al.*, 2013), but were recently revised to be clockwise based on relatively robust evidence for the pre-peak decompression and heating (Jiao *et al.*, 2013a; Yang *et al.*, 2014; Li & Wei, 2016, 2018; Lobjoie *et al.*, 2018; Li *et al.*, 2019).

The samples in this study were collected from the Tianpishan outcrop (40°46′46″N, 113°16′04″E) in the Jining complex (Fig. 1c). The rocks show prominent heterogeneity in decimetre to centimetre scale, with schlieren and gneissic structures composed of felsic leucocratic domains and ferromagnesian-rich melanocratic domains (Fig. 2a), indicating extensive partial melting during high-grade metamorphism (also see Santosh *et al.*, 2007b; Jiao & Guo, 2011; Li & Wei, 2018).

ANALYTIC METHODS

Mineral analyses were performed on a JEOL-8230 electron microprobe analyser (EMPA) and HR-Evolution laser Raman microscope at the Key Laboratory of Orogenic Belts and Crustal Evolution, Peking University, Beijing. Acceleration voltage and beam current were 15 kV and 10 nA, respectively. The beam was set to diameters of 1–2 μm, and counting times were 5 s on background and 10–15 s on peak. The SPI 53 minerals standard from SPI Supplies (U.S.) was used for the quantitative analysis, the PRZ correction was made at the final calibration stage, and other details are described in Li *et al.* (2018). The Raman spectroscopy was carried out using 532 nm excitation wavelength on the Ar-ion laser. The laser spot was focused to 1–2 μm, the accumulation time for spectra was 10 s, and the estimated spectral resolution was 0·7 cm^{-1}. The mineral phases were identified using the KIA® database software. Mineral formulas and site occupancies were determined for fixed oxygen anion amounts, with trivalent iron calculated by stoichiometric charge balance.

The image analyses for proportion of minerals and exsolved lamellae were performed using the ImageJ® software, to generate effective local compositions and reintegrate pre-exsolved homogeneous mineral compositions. To take perthite as an example, the mineral grains in a photomicrograph were cropped to suitable rectangles, and the exsolved lamellae were automatically distinguished, with their area proportions measured by particles summation. Other details are the same as those described in Hokada (2001).

In-situ zircon U–Th–Pb isotope analysis and cathodoluminescence (CL) imaging were carried out on sensitive high-resolution ion microprobe (SHRIMP) and JEOL JSM-6610A scanning electron microscope (SEM) equipped with Robinson CL detector respectively, at Research School of Earth Sciences, Australian National University, Canberra. The primary O_2 beam was focused to 10 μm in diameter, six scans of data were acquired in 20 min, and zircon Temora-2 was used as standard. Other details about the analytic procedures are similar to those described in Williams (1998) and Ireland & Williams (2003). Data were reduced using the Isoplot-4·15 Excel macro of Ludwig (2003).

PETROLOGIC ANALYSES

A representative sapphirine-bearing pelitic granulite sample 17TPS was selected for petrologic analyses (Fig. 2b). It consists of quartz (q), perthite (per), plagioclase (pl), garnet (g), sillimanite (sill), spinel (sp), sapphirine (sa), orthopyroxene (opx), biotite (bi), cordierite (cd) and Ti−Fe oxides. The rock is markedly heterogeneous on a centimetre scale (Fig. 2b, c), and can be divided into melanocratic domains rich in sillimanite (MD-s; Fig. 2c, d) or rich in orthopyroxene (MD-o; Fig. 2c, e), and leucocratic domains (LD; Fig. 2c, f). The mineral proportions for each type of domain are presented in Table 1.

The effective bulk-rock compositions of MD-s, MD-o and LD were generated by volume weighted integration of the constituent mineral compositions in local size (Fig. 2c) and presented in Table 2 together with the bulk-rock composition measured by X-ray fluorescence (XRF). MD-s contains high Al_2O_3, Fe_2O_3 and MgO, but low Na_2O and CaO with the highest A/CNK (see Table 2 for definition) of 5·6 and A/AFM of 0·50. In contrast, MD-o contains much higher Fe_2O_3 and MgO, and lower Al_2O_3 with A/CNK of 3·0 and A/AFM of 0·17. LD shows an Al-rich granitic composition with high SiO_2, Na_2O and K_2O, but low Fe_2O_3 and MgO with A/CNK of 1·3 and A/AFM of 0·40. MD-s, MD-o and LD have X_{Mg} of 0·47, 0·58 and 0·53, respectively. In the compiled A/AFM–X_{Mg} diagram (Fig. 3), the measured bulk-rock composition (labeled with XRF) is plotted between MD-s and LD, consistent with a rock that is dominated by these two domains and contains minor MD-o (Fig. 2c). All the effective compositions of the three types of domains fall on the compositional field of sapphirine-bearing granulites compiled from the Jining complex and other regions worldwide (Fig. 3).
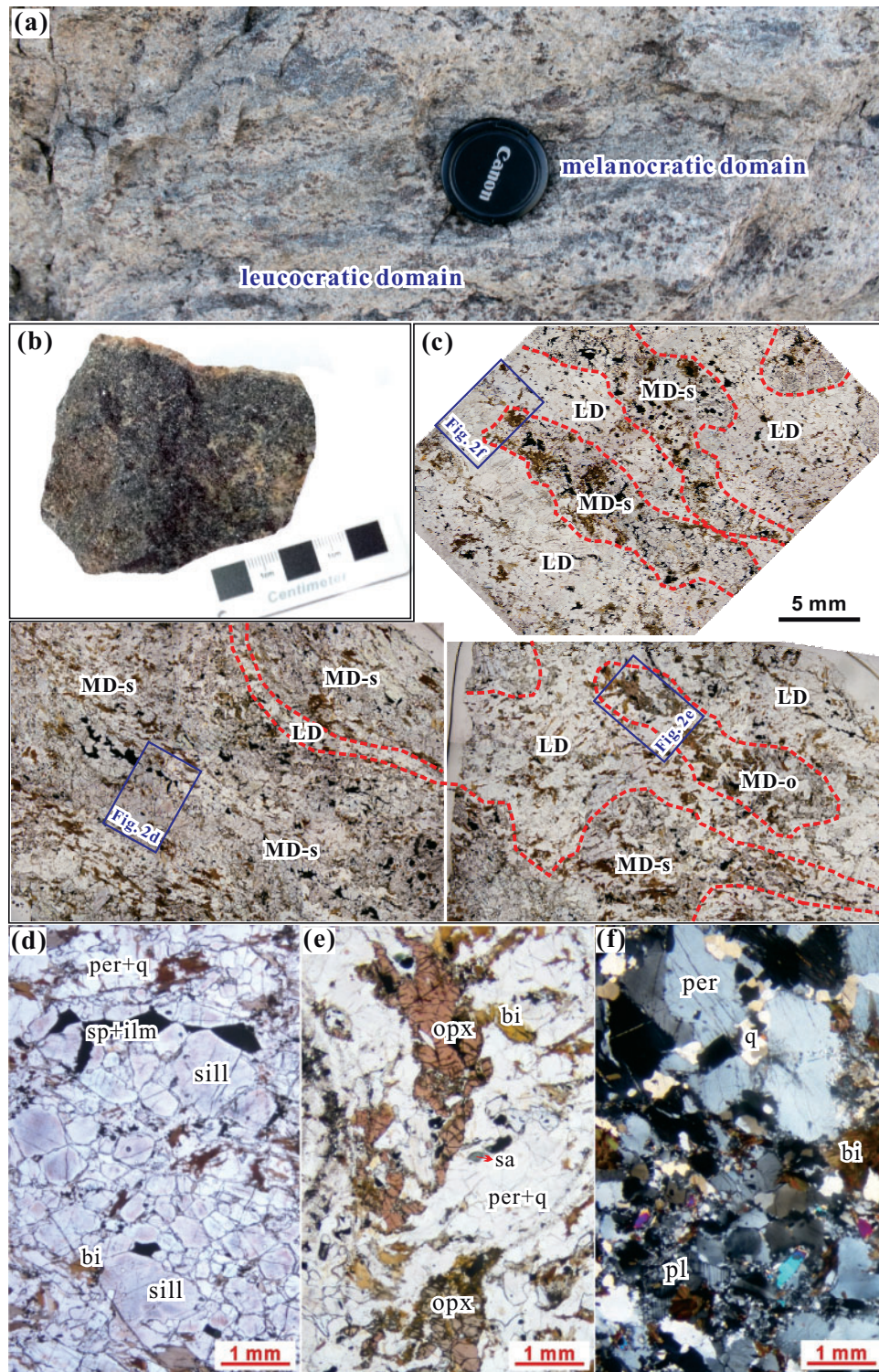
Fig. 2. (a) Field photograph of the Tianpishan outcrop. (b) Photograph of the hand specimen of the investigated sapphirine-bearing granulite. (c) Dissections showing the distribution of the three types of mineralogical or compositional domain in thin-sections. (d–f) Representative photographs of the three types of domain. MD-s, melanocratic domain rich in sillimanite; MD-o, melanocratic domain rich in orthopyroxene; LD, leucocratic domains.

Petrography and mineral chemistry of MD-s

MD-s mainly consists of sillimanite, garnet, perthite and quartz, with a small amount of sapphirine, spinel, plagioclase, orthopyroxene, biotite, cordierite and ilmenite.

Sillimanite shows prismatic and overgrown textures, and is sub-divided into two types. Type one (sill-I) is restricted to the core of prismatic sillimanite and has densely exsolved aciculae of hematite (Fig. 4a), which are 1–2 μm wide and oriented parallel to the *c*

Table 1: Mineral proportions of different domains (vol. %)

Domains	sill	g	opx	Sa	sp	per	pl	q	bi	cd	ilm
MD-s	17.4	15.4	1.8	0.4	3.7	19.2	0.5	24.3	6.7	9.6	1
MD-o	–	19.2	29.1	1.2	–	14.3	0.5	22.7	6.8	4.9	1.3
LD	2.8	6.1	–	–	–	46.3	12.5	26.9	3.8	1.2	0.4

Table 2: Bulk-rock analysis for sample 17TPS and effective compositions of different domains (wt %)

Sample	SiO_2	TiO_2	Al_2O_3	Fe_2O_3	MnO	MgO	CaO	Na_2O	K_2O	P_2O_5	LOI	A/CNK	A/AFM	X_{Mg}
17TPS	54.54	0.906	25.39	9.21	0.054	4.55	0.50	0.62	3.27	0.175	0.74	4.6	0.46	0.49
MD-s	55.19	0.747	26.89	9.26	–	4.22	0.58	0.63	2.47	–	–	5.6	0.50	0.47
MD-o	58.89	0.910	12.95	14.16	–	9.81	0.61	0.53	2.15	–	–	3.0	0.17	0.58
LD	69.32	0.324	17.46	2.33	–	1.34	1.97	3.12	4.15	–	–	1.3	0.40	0.53

Sample 17TPS was analysed by X-ray fluorescence (XRF) and the effective compositions were generated by volume-weighted integration of mineral compositions. $A/CNK = Al_2O_3/(CaO + Na_2O + K_2O)$, $A/AFM = (Al_2O_3 - CaO - Na_2O - K_2O)/(Al_2O_3 + FeO_{total} + MgO - CaO - Na_2O - K_2O)$, $X_{Mg} = MgO/(MgO + FeO_{total})$ in mole.
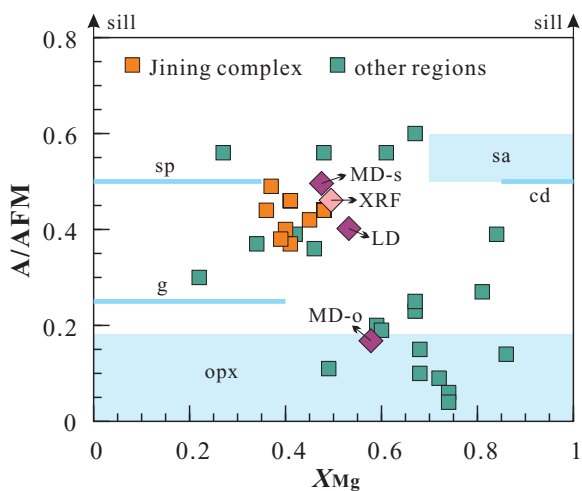

Fig. 3. A/AFM–X_{Mg} diagram showing the bulk-rock compositions of sapphirine-bearing UHT metapelites. Data are collected from the Jining complex (Shimizu *et al.*, 2013; Li & Wei, 2018; Lobjoie *et al.*, 2018) and other regions worldwide (Raith *et al.*, 1997; Osanai *et al.*, 1998; Brandt *et al.*, 2011; Rao *et al.*, 2012; Korhonen *et al.*, 2012). Also shown are the sketchy mineral plots. $A/AFM = (Al_2O_3–CaO–Na_2O– K_2O)/(Al_2O_3 + FeO_{total} + MgO–CaO–Na_2O–K_2O)$, $X_{Mg} = MgO/(MgO + FeO_{total})$ in mole.

crystallographic axis of sillimanite (Fleet & Arima, 1985). The host sillimanite contains Fe_2O_3 of 1.31–1.54 wt % (Table 3) and the exsolved hematite occupies 1.5–2.0 vol. % of the grain. Thus, pre-exsolution compositions of sill-I can be reintegrated to contain Fe_2O_3 up to 2.1–2..3 wt % (Fig. 5a). Type two sillimanite (sill-II) overgrows sill-I (Fig. 4a) and contains sapphirine, spinel, ilmenite and quartz as inclusions (Fig. 4a–c). It is exsolution-free and contains 1.29–1.79 wt % Fe_2O_3 (Table 3; Fig. 5a). Garnet occurs as anhedral grains that are 0.2–0.5 mm across, coexisting with sill-II (Fig. 4d) or as individual grains surrounded by fine-grained orthopyroxene (Fig. 4e), or cordierite coronae (Fig. 4f). It is characterized by X_{alm} [$= Fe^{2+}/ (Mg + Fe^{2+} + Ca + Mn)$, defined accordingly for other components] of 0.54–0.57, X_{prp} of 0.37–0.40, X_{gr} of 0.03–0.04 and X_{sps} of ~0.02

(Table 3), where X_{gr} increases clearly but other components fluctuate slightly from core to rim (Fig. 5b). Spinel is 0.05–0.25 mm across and occurs as inclusions in sill-II (or with a thin rind of sill-II; Fig. 4b, c) and perthite (Fig. 4g) or coexists with cordierite coronae around garnet (Fig. 4f). A few dark grains with a thin rind of sill-II have trellised exsolution lamellae of titanomagnetite (nearly pure ulvöspinel) in widths of 2–4 μm (Fig. 4i), which occupy ~3 vol. % of the total grain. The different types of spinel show similar X_{Al} [$= Al/(Al + Fe^{3+})$] of 0.94–0.99, variable X_{Mg} [$= Mg/(Mg + Fe^{2+})$] of 0.32–0.46, and low ZnO of 0.15–1.3 wt% with X_{Zn} [$= Zn/(Mg + Fe^{2+} + Zn)$] below 0.03 (Table 3). The dark grains with exsolution lamellae were reintegrated to contain ~1 wt % TiO_2. Sapphirine is 0.05–0.15 mm across and occurs as inclusions in sill-II (Fig. 4a, c). It shows X_{Mg} of 0.68–0.71 and Al^{IV} (tetrahedral Al in p.f.u.) of 0.12–0.18 (Table 3). Orthopyroxene occurs as fine grains that are 0.05–0.15 mm across, surrounding garnet or sill-II (Fig. 4d, e, h). It contains 5.25–6.03 wt % Al_2O_3 ($Al^{IV} = $ 0.13–0.14; Fig. 5c) and shows an X_{Mg} of 0.65–0.67 (Table 3). Perthite occurs as anhedral crystals that are 1–2 mm across. It has 13.2–16.6 vol. % of exsolved lamellae that are 2–4 μm in width, and occasionally has inclusions of spinel and ilmenite (Fig. 4g). The host sanidine has X_{or} [$= K/(Ca + Na + K)$] of 0.84–0.86 and X_{an} [$= Ca/(Ca + Na + K)$] below 0.01 and the exsolved lamellae have X_{an} of 0.28–0.30 and X_{or} below 0.01 (Table 3), which allows the reintegration of an original suprasolvus K-feldspar (ksp) with X_{or} of 0.68–0.72 and X_{an} of 0.05–0.06 (Fig. 5d). Plagioclase occurs as intersertal grains that are 0.1–0.5 mm across. It has X_{an} of 0.30–0.32 (Table 3). Biotite occurs as rounded inclusions mostly along the fractures in garnet, or as aggregated flakes with irregular and cuspate boundaries in the matrix commonly surrounding sill-II, garnet or orthopyroxene (Fig. 4b–f). The flakes in the matrix contain considerable TiO_2 content of 4.50–5.21 wt % and X_{Mg} of 0.75–0.76, while the inclusions in garnet show a higher X_{Mg} of 0.80–0.81 and slightly lower TiO_2 of 3.78–4.79 wt % than the former (Table 3). Cordierite commonly
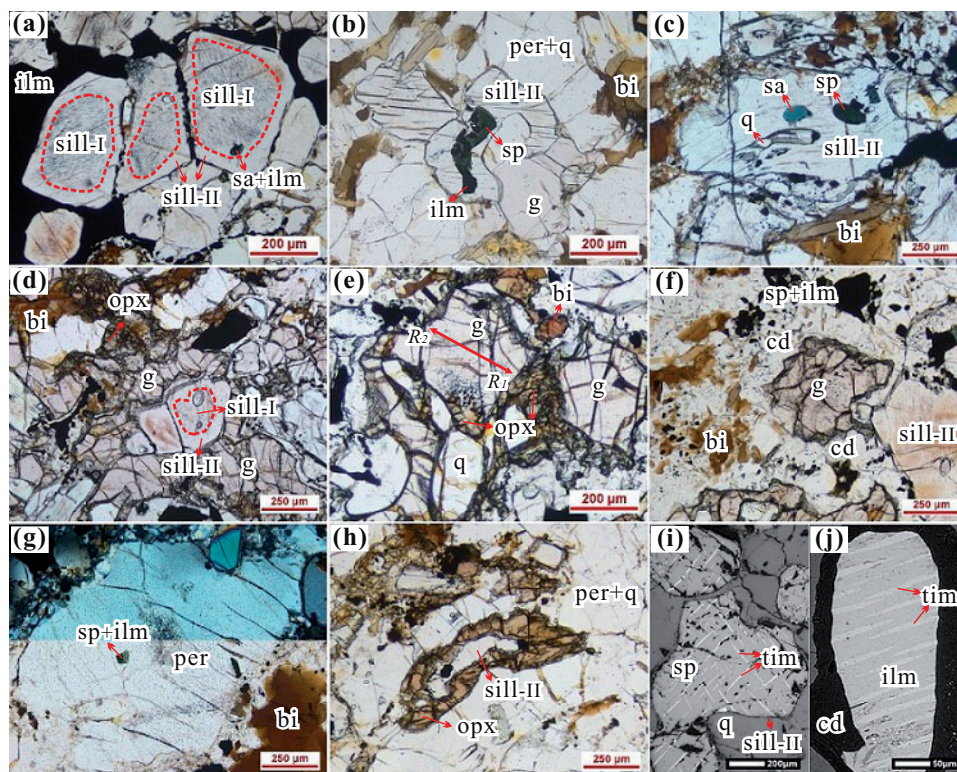
Fig. 4. Photomicrographs (a–h) and BSE images (i, j) showing the mineral textures in MD-s. (a) Sill-I with exsolved hematite aciculae is overgrown by exsolution-free sill-II that has inclusions of sapphirine and ilmenite. (b, c) Sill-II contains the inclusions of spinel, sapphirine, quartz and ilmenite; biotite occurs as flakes with irregular and cuspate boundaries. (d) Sill-II overgrows sill-I and coexists with garnet, followed by the sequential growth of orthopyroxene and biotite. (e) Fine-grained orthopyroxene occurs among garnet grains. (f) Cordierite together with spinel and ilmenite occurs as coronae around garnet and sill-II. (g) Perthite contains inclusions of spinel and ilmenite. (h) Orthopyroxene occurs as coronae around sill-II. (i) Dark spinel grains with a thin sill-II rind show trellised exsolution lamellae of titanomagnetite. (j) Ilmenite has exsolved titanomagnetite lamellae.

occurs as corona around garnet (Fig. 4f), and shows a uniform X_{Mg} of 0.82–0.84 (Table 3). Ilmenite (ilm) varies in size of 0.05–0.35 mm and commonly coexists with spinel or sapphirine within sill-II (Fig. 4a, b), and in the matrix (Fig. 4f). Some grains show exsolved titanomagnetite (tim) lamellae that are oriented and 5–10 μm wide (Fig. 4j). The host ilmenite contains 36.24–47.18 wt % TiO_2 with X_{ilm} ($FeTiO_3$ mole fraction) of 0.71–0.90, and the exsolved titanomagnetite contains 13.44–22.36 wt % TiO_2 with X_{usp} (Fe_2TiO_4 mole fraction) of 0.40–0.65 (Table 3).

According to the textural relations and mineral compositions mentioned above, the mineral parageneses in MD-s can be summarized as follows (Fig. 6). The peak assemblage is inferred to be characteristic of the coexistence of sapphirine, spinel and sill-I (Fig. 4a–c). Perthite should have been absent at the peak stage based on the fact that it contains the inclusions of spinel and ilmenite (Fig. 4g), but there is no perthite as an inclusion in sill-II like the minerals appearing in the peak assemblage (Fig. 4a–c). Sill-II together with garnet appears later (Fig. 4a–d), followed by orthopyroxene (Fig. 4e, h), and then biotite (Fig. 4d). Cordierite is inferred to appear latest from its coronal occurrence. In brief, the inferred sequence of mineral evolution in MD-

s is sa−sp−sill-I → per → sill-II/g → opx → bi → cd (Fig. 6).

Petrography and mineral chemistry of MD-o

MD-o mainly consists of orthopyroxene, garnet, perthite and quartz, with a small amount of sapphirine, plagioclase, biotite, cordierite and ilmenite.

Garnet occurs as anhedral grains that are 0.2–0.5 mm across (Fig. 7a). It shows X_{alm} of 0.58–0.62, X_{prp} of 0.32–0.36, X_{gr} of ∼0.03 and X_{sps} of ∼0.03 (Table 4), without evident compositional zoning. Sapphirine occurs as residual grains that are 0.1–0.3 mm across in felsic matrix (Fig. 7a, b). It is evidently nonuniform in composition, with sharply elevating Al^{IV} from core (0.02–0.11) to rim (0.16–0.24). It gives an X_{Mg} of 0.64–0.70, slightly increasing from core to rim (Table 4). Orthopyroxene occurs as medium-sized grains that are 1–2 mm across and is a dark red color (Fig. 7b, c). It gives an X_{Mg} of 0.63–0.65 and contains 6.75–9.46 wt % Al_2O_3, decreasing clearly from core to rim as shown by the Al^{IV} variance from 0.22 in the core to 0.17 in the rim (Table 4; Fig. 5c). Perthite occurs as anhedral crystals that are 1–2 mm across. It has 14.5–17.1 vol. % exsolved lamellae of widths of 2–5 μm The host sanidine has X_{or}

Table 3: Selected EMP analyses for minerals in MD-s

Minerals	sill-l-oc	sill-ll	g-c	g-r	sp-oc (sill-ll)	sp-el (sill-ll)	sp [cd]	sa	opx	per-oc	per-el	pl	bi	bi (g)	cd	ilm	tim
SiO_2	36.65	36.42	39.54	38.22	–	–	–	14.78	50.90	65.88	61.93	61.66	40.11	39.44	50.06	–	–
TiO_2	0.07	0.16	–	–	0.04	33.03	0.02	–	0.01	–	–	–	4.56	4.59	–	36.53	15.43
Al_2O_3	61.85	61.86	21.49	22.23	58.66	0.05	59.3	55.82	5.25	19.01	24.11	25.22	13.81	14.63	34.22	0.55	0.14
Cr_2O_3	–	–	–	–	0.37	0.10	0.41	–	–	–	–	–	–	–	–	0.10	0.29
FeO	1.39	1.61	27.35	27.00	30.85	60.06	30.27	13.16	21.21	–	–	–	9.86	8.53	4.33	53.56	75.16
MnO	–	–	0.73	0.86	0.05	0.02	0.08	0.03	0.20	–	–	–	0.01	0.00	0.26	0.68	0.00
MgO	–	–	10.18	10.24	8.87	0.00	9.01	14.12	22.61	–	–	–	17.54	19.08	10.88	0.23	0.00
CaO	–	–	1.13	1.52	–	–	–	–	0.08	0.13	5.75	6.37	–	–	–	–	–
Na_2O	–	–	–	–	–	–	–	–	0.01	1.53	8.25	7.96	0.13	0.11	–	–	–
K_2O	–	–	–	–	–	–	–	–	–	13.25	0.13	0.15	9.19	9.19	–	–	–
ZnO	–	–	–	–	1.3	–	0.9	–	–	–	–	–	–	–	–	–	–
Total	99.96	100.05	100.42	100.07	100.14	93.26	99.99	98.01	100.35	99.80	100.17	101.36	95.21	95.60	99.75	91.65	91.02
O	5	5	12	12	4	4	4	20	6	8	8	8	11	11	11	3	4
Si	0.99	0.99	3.02	2.92	–	–	–	1.84	1.87	3.00	2.74	2.70	2.91	2.83	4.99	–	–
Ti	0.00	0.00	–	–	0.00	0.99	0.00	–	0.00	–	–	–	0.25	0.25	–	0.74	0.47
Al	1.98	1.98	1.94	2.00	1.89	0.00	1.91	8.18	0.23	1.02	1.26	1.30	1.18	1.24	4.02	0.02	0.01
Cr	–	–	–	–	0.01	0.00	0.01	–	–	–	–	–	–	–	–	0.00	0.01
Fe^{3+}	0.03	0.04	0.03	0.15	0.10	0.01	0.08	0.15	0.03	–	–	–	0.00	0.00	0.01	0.49	1.05
Fe^{2+}	–	–	1.72	1.58	0.61	1.99	0.61	1.22	0.62	–	–	–	0.60	0.51	0.35	0.72	1.47
Mn	–	–	0.05	0.06	0.00	0.00	0.00	0.00	0.01	–	–	–	0.00	0.00	0.02	0.02	0.00
Mg	–	–	1.16	1.17	0.36	0.00	0.37	2.62	1.24	–	–	–	1.89	2.04	1.62	0.01	0.00
Ca	–	–	0.09	0.13	–	–	–	–	0.00	0.01	0.27	0.30	–	–	–	–	–
Na	–	–	–	–	–	–	–	–	0.00	0.14	0.71	0.68	0.02	0.02	–	–	–
K	–	–	–	–	–	–	–	–	–	0.77	0.01	0.01	0.85	0.84	–	–	–
Zn	–	–	–	–	0.03	–	0.02	–	–	–	–	–	–	–	–	–	–
Cat.	3	3	8	8	3	3	3	14	4	4.9	5.0	5.0	7.7	7.7	11	2	3
X(phase)	1.54	1.79	0.03	0.04	0.95		0.96	0.16	0.13	0.01	0.28	0.30	0.76	0.80	0.82	0.74	0.47
Y(phase)	–	–	0.40	0.43	0.37		0.37	0.68	0.67	0.85	0.01	0.01					

-oc, oikocryst; -el, exsolved lamella; c, core; r, rim; (sill-ll)/(g), the host mineral of an inclusion; [cd], the coexistent mineral. $X(sill) = X_{Al} = Al/(Al + Fe^{3+})$, $X(g) = X_{gr} = Ca/(Mg + Fe^{2+} + Ca + Mn)$, $X(sp) = X_{Al} = Al/(Al + Fe^{3+})$, $X(sa/opx) = Al^{IV}$, $X(per/pl) = X_{an} = Ca/(Ca + Na + K)$, $X(ilm) = X_{ilm} = Fe^{2+}/(Fe^{2+} + Fe^{3+}/2)$, $X(tim) = X_{usp} = Ti/(Ti + Fe^{3+}/2)$, $Y(g/sp/sa/opx/bi/cd) = X_{Mg} = Mg/(Mg + Fe^{2+})$, $Y(per/pl) = X_{or} = K/(Ca + Na + K)$. –, not analysed.
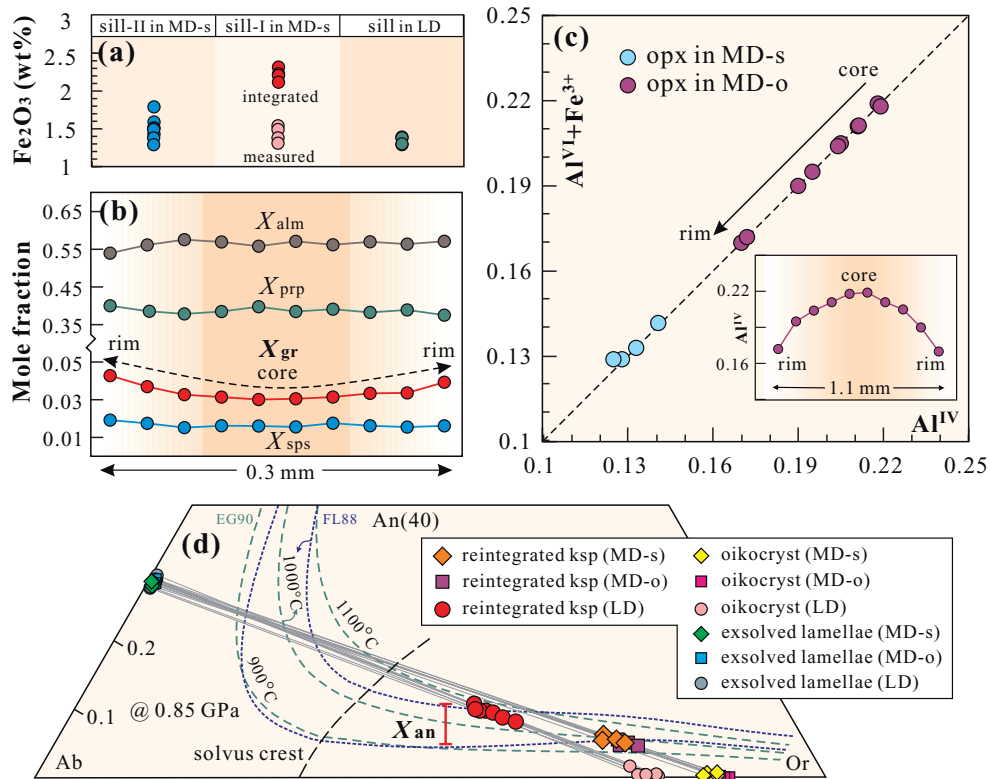
Fig. 5. Compositional diagrams for minerals. (a) A binary diagram showing the Fe_2O_3 content variations of sillimanite in different types. (b) Zoning profile of X_{alm} (= Fe^{2+}/(Fe^{2+} + Mg + Ca + Mn)), defined accordingly for other components), X_{prp}, X_{gr} and X_{sps} for garnet in MD-s. (c) Coupled compositional plots of (Al^{VI} + Fe^{3+}) versus Al^{IV} for orthopyroxene, subjoined with Al^{IV} zoning profile for orthopyroxene in MD-o. (d) Compositional plots of measured perthite and reintegrated K-feldspar. Isotherms at 0·85 GPa are based on the models of Fuhrman & Lindsley (1988) and Elkins & Grove (1990).

Fig. 6. A summary of the paragenesis of minerals based on petrography and mineral chemistry. The solid lines show the presence of minerals, and the dashed lines indicate the possible presence of a mineral.

of 0·86–0·88 and X_{an} below 0·01 and the exsolved lamellae have X_{an} of 0·28–0·29 and X_{or} of ~0·01 (Table 4), which allows to reintegrate an original supra-solvus K-feldspar (ksp) with X_{or} of 0·71–0·74 and X_{an} of 0·05–0·06 (Fig. 5d). Plagioclase occurs as intersertal grains that are 0·1–0·5 mm across. It has an X_{an} of 0·32–0·33 (Table 4). Biotite occurs as aggregated flakes commonly surrounding garnet or orthopyroxene (Fig. 7a, c). It gives an X_{Mg} of 0·63–0·66 and TiO_2 of 3·9–4·08 wt % (Table 4). Cordierite occurs as coronae around garnet (Fig. 7a), with an X_{Mg} of 0·84–0·86 (Table 4).

The above mentioned textural relations and mineral compositions for MD-o suggest that the peak assemblage is marked by the presence of orthopyroxene and sapphirine, which are separated by perthite and quartz (Fig. 7b). This textural relation also implies that perthite may have formed later than the peak minerals. Garnet is inferred to be excluded from peak assemblage with a reference of its paragenesis in MD-s. Biotite is clearly a later growth (Fig. 7c) and cordierite should be the latest. In brief, the inferred sequence of mineral evolution in MD-o is sa−opx → per → g → bi → cd (Fig. 6).

Petrography and mineral chemistry of LD

LD mainly consists of perthite, plagioclase and quartz, with a small amount of sillimanite, garnet, biotite, cordierite and ilmenite.

Sillimanite without any exsolution occurs as interstitial grains or inclusions in perthite (Fig. 7d). It shows uniform compositions and contains 1·29–1·39 wt % Fe_2O_3 (Table 4). Garnet occurs as fine grains in the felsic matrix. It shows X_{alm} of 0·57–0·60, X_{prp} of 0·35–0·38, X_{gr} of ~0·03 and X_{sps} of ~0·02 (Table 4), and the cores show slightly lower X_{gr}. Perthite occurs as anhedral grains that are 1–2 mm across. It has 21·7–33·2 vol. % of exsolved lamellae with widths of 5–10 μm, and some grains have inclusions of sillimanite, plagioclase or ilmenite (Fig. 7d, e). The host sanidine has X_{or} of 0·74–
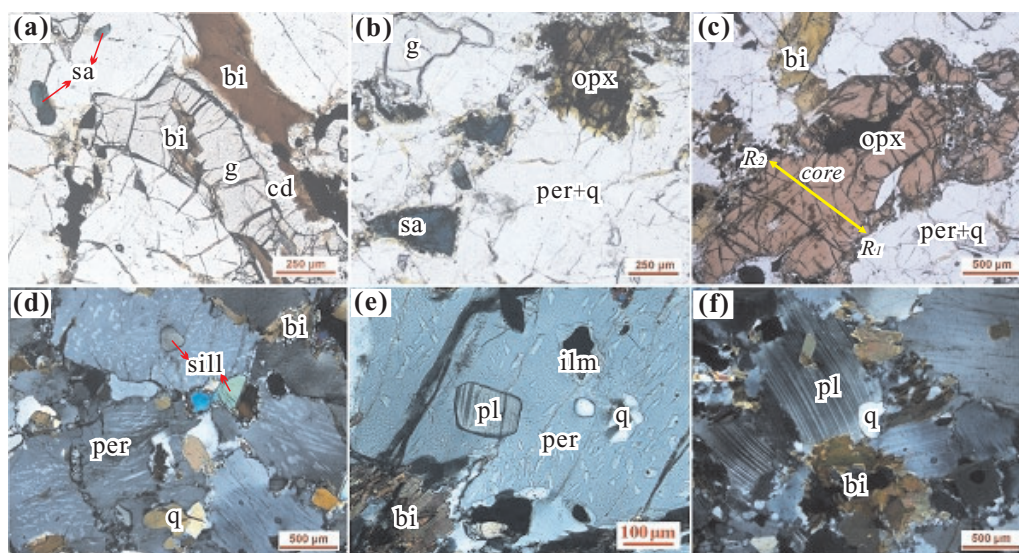
Fig. 7. Photomicrographs showing the mineral textures in MD-o (a–c) and LD (d–f). (a) Garnet embayed by cordierite and biotite. (b) Sapphirine, orthopyroxene and garnet occur as isolated grains in the matrix of perthite and quartz, with biotite formed later. (c) A dark red-colored orthopyroxene grain is in the matrix of perthite and quartz, with biotite formed later. (d) Sillimanite without any exsolution occurs as inclusions in perthite and grains in matrix. (e) Perthite contains the inclusions of plagioclase, ilmenite and quartz. (f) Biotite occurs as aggregated flakes among plagioclase.

0·79 and X_{an} below 0·02, the exsolved lamellae have X_{an} of 0·28–0·30 and X_{or} below 0·01 (Table 4), and the reintegrated composition for supra-solvus K-feldspar shows X_{or} of 0·50–0·57 and X_{an} of 0·08–0·11 (Fig. 5d). Plagioclase occurs mainly as anhedral crystals of 0·5–1 mm across and occasionally as inclusions within perthite (Fig. 7e, f). It shows uniform compositions and has X_{an} of 0·31–0·33 (Table 4), which slightly decreases from core to rim in some grains. Biotite occurs as aggregated flakes in the interstices among feldspars (Fig. 7d−f). It gives an X_{Mg} of ~0·64 and TiO_2 of 3·87–4·10 wt % (Table 4). Cordierite occurs as very thin coronae around garnet and shows X_{Mg} of 0·84–0·86 (Table 4).

In LD, perthite is inferred to be formed later than sillimanite and plagioclase according to the textures in Fig. 7d, e, and thus, may be absent at the peak stage (Fig. 6). Biotite is formed much later based on its intersertal occurrences as fine flakes (Fig. 7d−f).

PHASE EQUILIBRIA MODELLING

For the mineral compositions mentioned above, a model system NCKFMASHTO (Na_2O–CaO–K_2O–FeO–MgO–Al_2O_3–SiO_2–H_2O–TiO_2–Fe_2O_3) was chosen for phase equilibria modelling. The calculations were performed using THERMOCALC 3·40 (Powell & Holland, 1988) with dataset ds62 (Holland & Powell, 2011). Mineral activity–composition relationships are the same as those in White *et al.*, (2014*a*). The effective rock compositions for the three compositional domains (Table 5) are normalized according to the model system and used for the modelling. The H_2O content was adjusted to ensure that the final-phase assemblage occurs just above the solidus (e.g. Korhonen *et al.*, 2011, 2012), and the Fe^{3+}/Fe value was properly adjusted using $T − X_{Fe}^{3+}$ diagrams. As the sillimanite commonly contains non-negligible Fe_2O_3, we propose a new ferric-sillimanite $\alpha − X$ model (see the Appendix) to investigate the UHT phase equilibria.

Pseudosections for MD-s

The P–T pseudosection for MD-s was calculated over the P–T window of 0·5–1·1 GPa and 800–1200 °C with quartz, ilmenite and sillimanite in excess. It is contoured with the isopleths of X_{an}(ksp), X_{gr}(g), Al^{IV}(opx) and Fe_2O_3(sill) for the relevant mineral assemblages (Fig. 8a). The inferred peak assemblage characteristic of sa + sp + sill-I is predicted to stabilize at temperatures above 1120 °C at pressures of 0·8–0·9 GPa. The reintegrated Fe_2O_3 of 2·1–2·3 wt % in sill-I yields consistent temperature conditions of 1110–1140 °C. Upon cooling, the observed sequential appearance of per (ksp) → sill-II/g → opx → bi can be well documented. Firstly, the formation of K-feldspar together with plagioclase and quartz is predicted to occur at temperatures from ~1120 °C to ~1045 °C and it is attributed to the crystallization of melt, which has a trivial influence on the modes of sapphirine, spinel and sillimanite shown as C in Fig. 8b. The reintegrated perthite composition with $X_{an} = 0·05$–0·06 is also consistent with this temperature range. Note that the initial crystallization temperature of the melt that contains minor amounts of water is only 10 °C lower than the dry solidus calculated for the rock. Secondly, the notable growth of sill-II accompanied with the appearance of garnet at the expense of sapphirine, spinel and quartz [sa (+ sp) + q = g + sill-II] proceeds from ~1045 °C to ~1010 °C (R1 in Fig. 8b). The

Table 4: Selected EMP analyses for minerals in MD-o and LD

Minerals	MD-o										LD								
	g	sa-c	sa-r	opx-c	opx-r	per-oc	per-el	pl	bi	cd	sill	sill (per)	G	per-oc	per-el	pl	pl (per)	bi	cd
SiO_2	38.86	15.43	14.63	48.46	49.64	65.09	61.55	60.53	37.49	50.17	36.99	36.85	39.69	65.25	61.61	60.41	61.51	37.05	51.06
TiO_2	–	–	–	0.05	0.05	–	–	–	3.90	–	0.01	0	–	–	–	–	–	4.10	–
Al_2O_3	21.07	56.22	59.81	9.46	7.63	18.67	24.72	25.72	14.70	32.89	62.02	62.22	22.51	18.80	25.00	25.52	25.52	14.27	33.83
FeO	28.37	13.23	11.62	21.62	21.93	–	–	–	14.05	3.95	1.24	1.25	27.95	–	–	–	–	14.66	3.63
MnO	1.52	0.03	0.03	0.12	0.10	–	–	–	0.18	0.04	–	–	0.89	–	–	–	–	0.15	0.04
MgO	9.00	14.37	14.60	20.78	21.04	–	–	–	15.13	11.42	–	–	9.72	–	–	–	–	14.50	11.32
CaO	1.03	–	–	0.04	0.07	0.04	5.88	6.88	–	–	–	–	1.20	0.32	6.19	6.51	6.55	–	–
Na_2O	–	–	–	0	0	1.60	8.11	7.44	0.11	–	–	–	–	2.57	8.30	7.75	7.43	0.05	–
K_2O	–	–	–	–	–	14.26	0.14	0.17	9.27	–	–	–	–	12.09	0.12	0.17	0.16	9.61	–
Total	99.85	99.34	100.70	100.53	100.46	99.66	100.40	100.74	94.86	98.47	100.26	100.32	101.96	99.03	101.22	100.36	101.17	94.45	99.88
O	12	20	20	6	6	8	8	8	11	11	5	5	12	8	8	8	8	11	11
Si	3.01	1.89	1.76	1.78	1.83	3.00	2.72	2.67	2.80	5.05	1.00	0.99	2.99	3.00	2.71	2.68	2.70	2.80	5.05
Ti	–	–	–	0.00	0.00	–	–	–	0.22	–	0.00	0.00	–	–	–	–	–	0.23	–
Al	1.93	8.12	8.46	0.41	0.33	1.01	1.29	1.34	1.29	3.90	1.97	1.98	2.00	1.02	1.29	1.33	1.32	1.27	3.95
Fe^{3+}	0.05	0.09	0.03	0.03	0.01	–	–	–	0.00	0.00	0.03	0.03	0.02	–	–	–	–	0.00	0.00
Fe^{2+}	1.79	1.26	1.14	0.64	0.67	–	–	–	0.88	0.33	–	–	1.75	–	–	–	–	0.93	0.30
Mn	0.10	0.00	0.00	0.00	0.00	–	–	–	0.01	0.00	–	–	0.06	–	–	–	–	0.01	0.00
Mg	1.04	2.63	2.61	1.14	1.16	–	–	–	1.68	1.71	–	–	1.09	–	–	–	–	1.63	1.67
Ca	0.09	–	–	0.00	0.00	0.00	0.28	0.33	–	–	–	–	0.10	0.02	0.29	0.31	0.31	–	–
Na	–	–	–	0.00	0.00	0.14	0.70	0.64	0.02	–	–	–	–	0.23	0.71	0.67	0.63	0.01	–
K	–	–	–	–	–	0.84	0.01	0.01	0.88	–	–	–	–	0.71	0.01	0.01	0.01	0.93	–
Cat.	8	14	14	4	4	5.0	5.0	5.0	7.8	11	3	3	8	5.0	5.0	5.0	5.0	7.8	11
X(phase)	0.03	0.11	0.24	0.22	0.17	0.00	0.28	0.33	0.66	0.84	1.38	1.39	0.03	0.02	0.29	0.31	0.32	0.64	0.85
Y(phase)	0.37	0.68	0.70	0.64	0.63	0.88	0.01	0.01	0.84	–	–	–	0.38	0.74	0.01	0.01	0.01	0.66	–

-oc, oikocryst; -el, exsolved lamella; c, core; r, rim; (per), perthite inclusions. $X(g) = X_{gr} = Ca/(Mg + Fe^{2+} + Ca + Mn)$, $X(sa/opx) = Al^{IV}$, $X(per/pl) = X_{an} = Ca/(Ca + Na + K)$, $X(sa/opx) = Al^{IV}$, $X(per/pl) = X_{an} = Ca/(Ca + Na + K)$, $X(sill) = Fe_2O_3$, $Y(g/sa/opx/bi/cd) = X_{Mg} = Mg/(Mg + Fe^{2+})$, $Y(per/pl) = X_{or} = K/(Ca + Na + K)$. –, not analysed.

Table 5: Normalized molar proportions used for phase equilibria modelling (mol %)

Domains		Figures		H_2O^*	SiO_2	Al_2O_3	CaO	MgO	FeO_{total}	K_2O	Na_2O	TiO_2	O^*
MD-s		Fig. 8		0·25	61·22	17·58	0·69	6·98	7·72	1·75	0·68	0·62	2·51
		Fig. 9	$(X_{Fe}^{3+} = 0.2)$	0·25	62·31	17·9	0·70	7·10	7·86	1·78	0·69	0·63	0·79
			$(X_{Fe}^{3+} = 0.9)$	0·24	60·65	17·42	0·68	6·91	7·65	1·73	0·67	0·61	3·44
MD-o		Fig. 10		0·25	59·98	7·77	0·66	14·89	10·85	1·39	0·52	0·70	2·99
		Fig. 11a	(A/AFM = 0·1)	0·25	61·76	5·03	0·68	15·34	11·17	1·43	0·54	0·72	3·08
			(A/AFM = 0·6)	0·20	48·19	25·90	0·53	11·97	8·72	1·12	0·42	0·56	2·40
		Fig. 11b	$(X_{Mg} = 0.46)$	0·25	59·98	7·77	0·66	9·10	16·65	1·39	0·52	0·70	2·99
			$(X_{Mg} = 0.90)$	0·25	59·98	7·77	0·66	17·80	7·95	1·39	0·52	0·70	2·99
LD		Fig. 12		0·05	75·50	11·21	2·29	2·17	1·91	2·88	3·29	0·26	0·44
		Fig. 13		0·05	78·06	11·59	2·37	2·24	1·97	2·98	0·00	0·27	0·46
				0·05	74·16	11·01	2·25	2·13	1·88	2·83	5·00	0·26	0·43

*, adjusted proportions; $X_{Fe}{}^{3+} = Fe^{3+}/Fe = 2O/FeO_{total}$; A/AFM and X_{Mg} see Fig. 11.
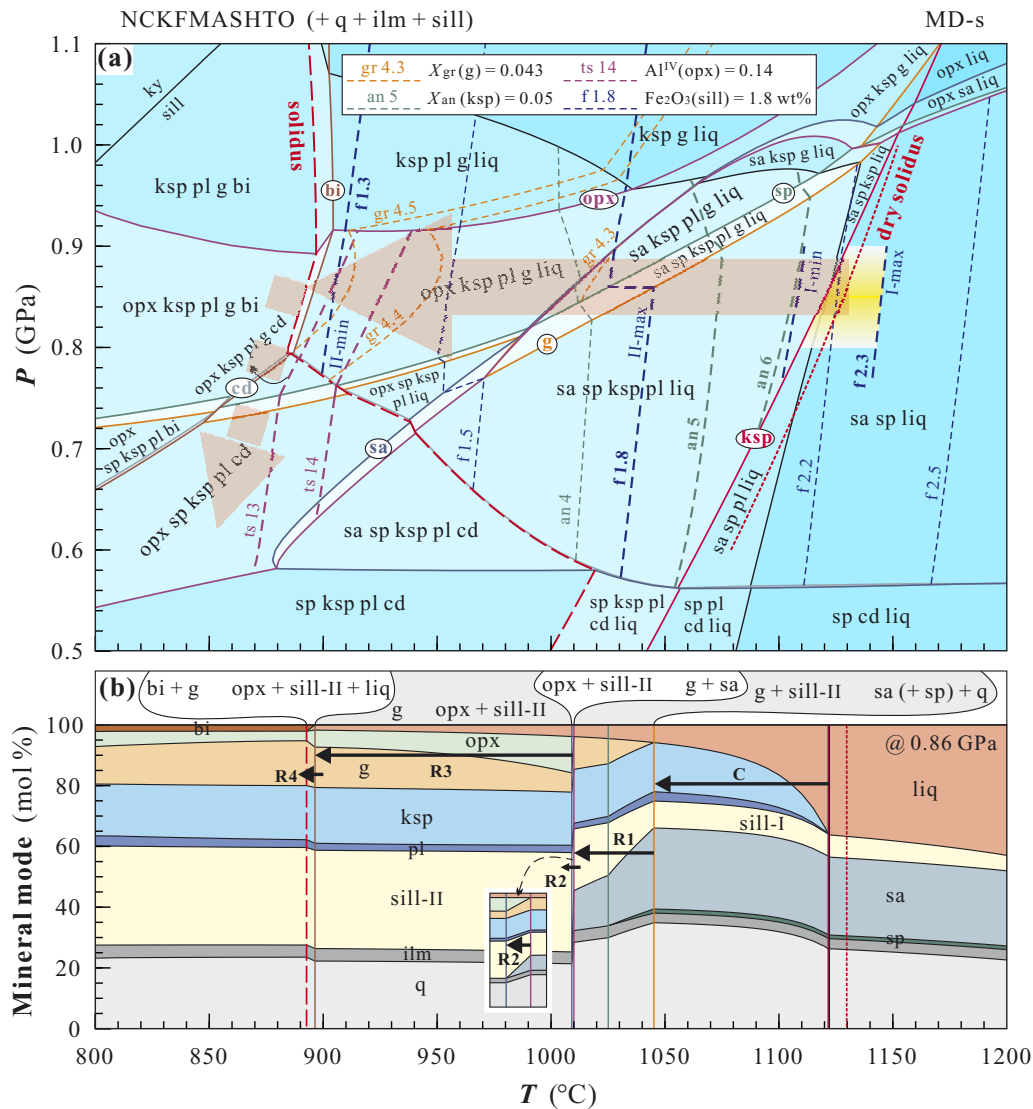

Fig. 8. (a) A *P–T* pseudosection with the proposed peak conditions and *P–T* path. It is shaded with increasing color depth for the fields of increasing degrees of freedom. The compositional isopleths of garnet, orthopyroxene, K-feldspar and sillimanite are presented for the relevant assemblages, where the bold curves refer to the key isopleths for the measured values, with the maximum and minimum Fe_2O_3 in the two types of sillimanite labelled as I-max, I-min, II-max and II-min, respectively. The dry solidus was calculated in H_2O-free subsystem. (b) A *T*-Mode diagram showing the variation of mineral and melt mode (on one-oxide mol %), and the temperature ranges of melt crystallization (C) and crucial metamorphic reactions (R1–R4) along the cooling path at 0·86 GPa.

measured maximum Fe_2O_3 of 1·8 wt % in sill-II happens to plot within the temperature range for reaction R1. Thirdly, the appearance of orthopyroxene coupled with the further growth of sill-II at the expense of sapphirine and garnet (sa + g = opx + sill-II) may occur at a temperature of ∼1010 °C (R2 in Fig. 8b), which is followed by a reaction opx + sill-II = g to ∼900 °C (R3 in Fig. 8b), responsible for the further growth of garnet. The measured Al^{IV} (0·13–0·14) in orthopyroxene and Fe_2O_3 (1·3–1·5 wt %) in sill-II yield temperatures of 900–950 °C, consistent with the later evolution during this sub-stage. And fourthly, the formation of biotite (together with garnet) at the expense of melt and orthopyroxene (liq + opx + sill-II = bi + g) occurs at ∼900 °C (R4, in Fig. 8b), which terminates at the fluid-absent solidus. The above post-peak cooling evolution may have been followed by a decompression under sub-solidus conditions as indicated by the formation of cordierite coronae around garnet (Fig. 4f).

The core-rim zoning in garnet with increasing X_{gr} (Fig. 5b) also provides evidence for the cooling process mentioned above, according to the changing trend of $X_{gr}(g)$ isopleths in Fig. 8a, but the measured values of X_{gr} cannot be well plotted in the pseudosection. This is probably because (1) the garnet core may indicate higher temperatures if its stability field is expanded with the incorporation of MnO (Mahar *et al.*, 1997; Wei *et al.*, 2004; White *et al.*, 2014b), and (2) the plots of X_{gr} may have been affected by small variation in bulk-rock composition, such as CaO content (e.g. Dong *et al.*, 2018).

In Fig. 8a, the isopleths of the Fe_2O_3(sill) show steep slopes in most assemblages. As the Fe_2O_3(sill) may be influenced by the oxygen fugacity, we calculated a $T - X_{Fe}^{3+}$ pseudosection at 0·86 GPa (Fig. 9) to investigate the effects of bulk-rock X_{Fe}^{3+} on the phase relations. Figure 9 shows that the Fe_2O_3(sill) markedly increases with increasing X_{Fe}^{3+} in the fields with X_{Fe}^{3+} below ∼0·4, while in the fields with high X_{Fe}^{3+} values, the Fe_2O_3(sill) is mainly governed by temperature. Although the Fe_2O_3(sill) isopleths may indicate lower temperatures with increasing X_{Fe}^{3+}, the reintegrated Fe_2O_3 of 2·1–2·3 wt % in sill-I can yield temperatures about 1100 °C for the possible maximum X_{Fe}^{3+} value (∼0·76) that can stabilize the inferred spinel-bearing peak assemblage.

Pseudosections for MD-o

The *P–T* pseudosection for MD-o was calculated over the *P–T* window of 0·5–1·1 GPa and 800–1200 °C, with quartz and ilmenite in excess, which was contoured with the X_{an}(ksp) and Al^{IV}(opx) values for the relevant assemblages (Fig. 10a). The inferred peak assemblage marked by sa + opx is predicted to be stable at temperatures above 1120 °C at 0·8–0·9 GPa. The post-peak evolution along an isobaric cooling path is predicted to be marked by (1) the formation of K-feldspar together with plagioclase and quartz from ∼1120 °C to ∼1040 °C (C in Fig. 10b), representing the crystallization of melt with a slight variation in the mode of sapphirine and orthopyroxene; (2) the growth of garnet at the expense of sapphirine and orthopyroxene (sa + opx = g, R1 in
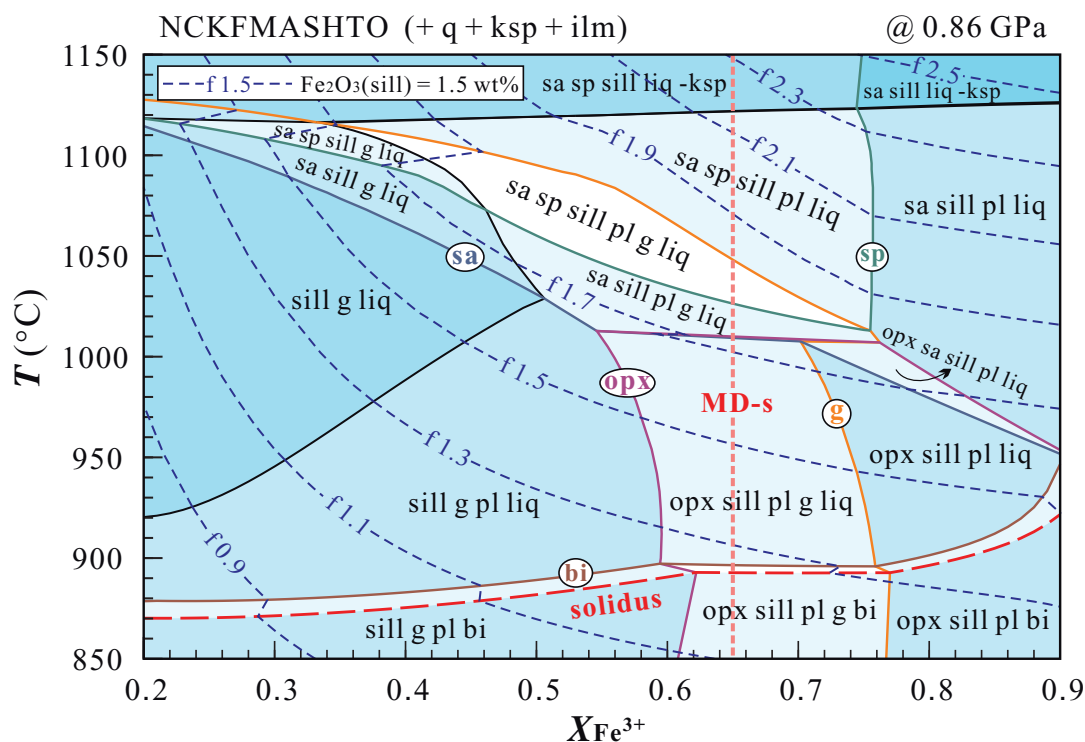

Fig. 9. A $T - X_{Fe}^{3+}$ pseudosection for MD-s calculated at 0·86 GPa showing especially the variation of the Fe_2O_3(sill) with the bulk-rock X_{Fe}^{3+} (= Fe^{3+}/Fe) values. Others are the same as in Fig. 8a.

Fig. 10. (a) A *P–T* pseudosection with the proposed peak conditions and *P–T* path. Others are the same as in Fig. 8a. (b) A *T*-Mode diagram showing the variation of mineral and melt mode, and the temperature ranges of melt crystallization (C) and crucial metamorphic reactions (R1 and R2) along the cooling path at 0·86 GPa.

Fig. 10b) from ~1040 °C to ~900 °C; and (3) the growth of biotite (together with garnet) with the expense of melt, orthopyroxene and sapphirine (liq + opx + sa = bi + g, R2 in Fig. 10b) from ~900 °C to the fluid-absent solidus. A further evolution dominated by decompression in sub-solidus conditions can be inferred from the formation of cordierite coronae around garnet (Fig. 7a). The measured core-rim zoning with decreasing Al^{IV} (0·22 → 0·17) in orthopyroxene is calculated to record a temperature decrease from ~1120 °C to ~990 °C (Fig. 10a), consistent with the conditions of the peak stage and post-peak cooling to the apparent growth of garnet. The reintegrated perthite composition with X_{an} = 0·05–0·06 yields temperatures of 1080–1110 °C, in good accordance with the crystallization of K-feldspar.

As shown in Fig. 10a, the amount of Al^{IV} in orthopyroxene is a good thermometer, but the slope of the isopleth may vary somewhat with respect to changing mineral assemblages. To investigate the behavior of Al^{IV}(opx) isopleths, we calculated T–A/AFM and T–X_{Mg} pseudosections at 0·86 GPa (Fig. 11). Phase relations in

Fig. 11a suggest that orthopyroxene is stable in the fields with A/AFM below 0·34–0·55, sapphirine is present in the fields with A/AFM above 0·15 and sillimanite stabilizes when the A/AFM is greater than 0·27–0·55 (depending on temperature). The Al^{IV}(opx) increases linearly as temperature increases, slightly influenced by the bulk-rock A/AFM in the sapphirine-present fields. In contrast, it increases only as the bulk-rock A/AFM increases in the sapphirine-absent fields. The value of Al^{IV}(opx) = 0·14 (Al_2O_3 = 6 wt %) can yield temperatures greater than 900 °C (Fig. 11a). The T–X_{Mg} pseudosection (Fig. 11b) shows that orthopyroxene and sapphirine are stable in the fields of high X_{Mg} while garnet stabilizes in the fields of low X_{Mg}. Although the Al^{IV}(opx) increases as temperature elevates in all the orthopyroxene-bearing assemblages, it clearly decreases with increasing X_{Mg} in the sapphirine-present fields but shows an inverse trend in the sapphirine-absent fields. The measured maximum Al^{IV}(opx) (0·22) can yield 1120 °C for the composition of MD-o (X_{Mg} = 0·75), while defining a lower temperature
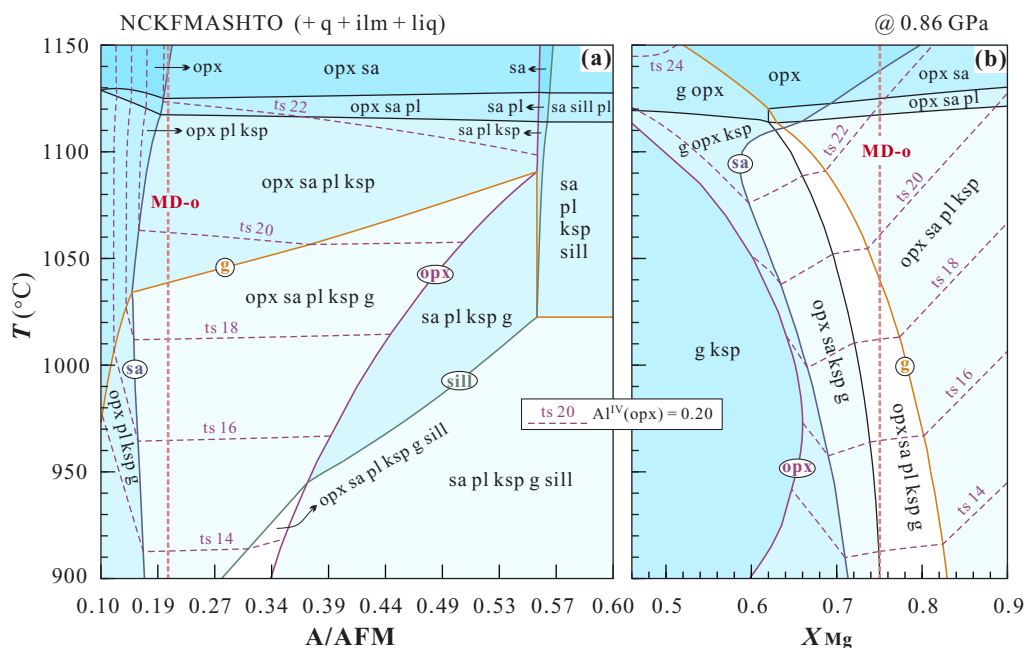
Fig. 11. (a) A $T - A/AFM$ pseudosection (note the nonlinear abscissa) and (b) a $T - X_{Mg}$ pseudosection, calculated at 0.86 GPa based on the composition of MD-o. The pseudosections are contoured with $Al^{IV}(opx)$, and shaded with increasing color depth for the fields with increasing degrees of freedom. $A/AFM = (Al_2O_3–CaO–Na_2O–K_2O)/(Al_2O_3 + FeO + MgO–CaO–Na_2O–K_2O)$, $X_{Mg} = MgO/(MgO + FeO)$ in mole.

of $\sim1075\,°C$ as X_{Mg} reduces to ~0.6. Note that an $Al^{IV}(opx)$ of 0.14 ($Al_2O_3 = 6$ wt %) can yield temperatures greater than 900 °C when X_{Mg} is between 0.6–0.9 (Fig. 11b).

Pseudosections for LD

The $P–T$ pseudosection for LD was calculated over the $P–T$ window of 0.5–1.1 GPa and 800–1200 °C, with quartz and ilmenite in excess, which was contoured with the $X_{an}(ksp)$, $X_{an}(pl)$ and $Fe_2O_3(sill)$ for the relevant fields (Fig. 12a). According to Kriegsman (2001), LD is dominated by segregated melts, which can yield temperatures up to 1140 °C at fixed pressures of 0.8–0.9 GPa (Fig. 12b), slightly above the dry solidus calculated for the rock, and consistent with the inferred K-feldspar-absent peak assemblage. The crystallization of melt during cooling is characterized by the formation of K-feldspar + quartz ± plagioclase at temperatures ranging from $\sim1140\,°C$ to $\sim1120\,°C$ (C in Fig. 12b), in accordance with the textural relations where sillimanite and plagioclase occur as inclusions in perthite (Fig. 7d, e). In this crystallization process, the amount of melt is sharply reduced from ~55 mol % to ~6 mol % (Fig. 12b). The further cooling evolution is dominated by the increase of plagioclase and the decrease of K-feldspar (ksp = pl, R1 in Fig. 12b) between 1120 °C and 910 °C, where garnet and sillimanite are not involved, and the melt mode is slowly reduced. Biotite growth occurs at $\sim910\,°C$ and terminates at the fluid-absent solidus (R2 in Fig. 12b). The reintegrated perthite composition with $X_{an} = 0.08$–0.11 is well consistent with the temperatures above 1100 °C. The measured $X_{an} = 0.31$–0.33 in plagioclase is

roughly in agreement with the inferred cooling conditions (Fig. 12a), although the $X_{an}(pl)$ isopleths irregularly fluctuate in the $P–T$ field. The measured $Fe_2O_3 = 1.3$–1.4 wt % in sillimanite recorded temperatures of 990–1030 °C (Fig. 12a). A decompression under the sub-solidus conditions can be inferred by the occurrence of cordierite coronae around garnet.

In Fig. 12a, the $X_{an}(ksp)$ isopleths show steep slopes and are a good temperature indicator. To investigate the influence of bulk-rock compositions on the $X_{an}(ksp)$, we calculated a $T - M(Na_2O)$ pseudosection at 0.86 GPa in Fig. 13. It shows that the $X_{an}(ksp)$ is dependent not only on temperatures, but also considerably on the bulk-rock Na_2O contents. For a given $X_{an}(ksp)$ value, it can yield much higher temperature estimates in Na_2O-lower rocks than in Na_2O-higher rocks.

ZIRCON GEOCHRONOLOGY

Thirty zircon grains in sample 17TPS (MD-s) were selected from thin-section and checked by energy dispersive spectrometer (EDS) for dating. Zircon commonly occurs as inclusions in perthite, sillimanite and biotite (Fig. 14a). Most grains are oval and 20–35 μm in size. They show intermediate and structureless luminescence, suggesting a high-grade metamorphic genesis (e.g. Corfu *et al.*, 2003). Their Th/U ratios range from 0.01–1.07 except one grain in sillimanite that has high Th/U = 3.12 (Table 6). Eleven grains were rejected due to high common lead in them, or forming outliers, and the other 19 grains were subdivided into three groups based on their textural relations. Seven zircon grains included in perthite yield $^{207}Pb/^{206}Pb$ ages from
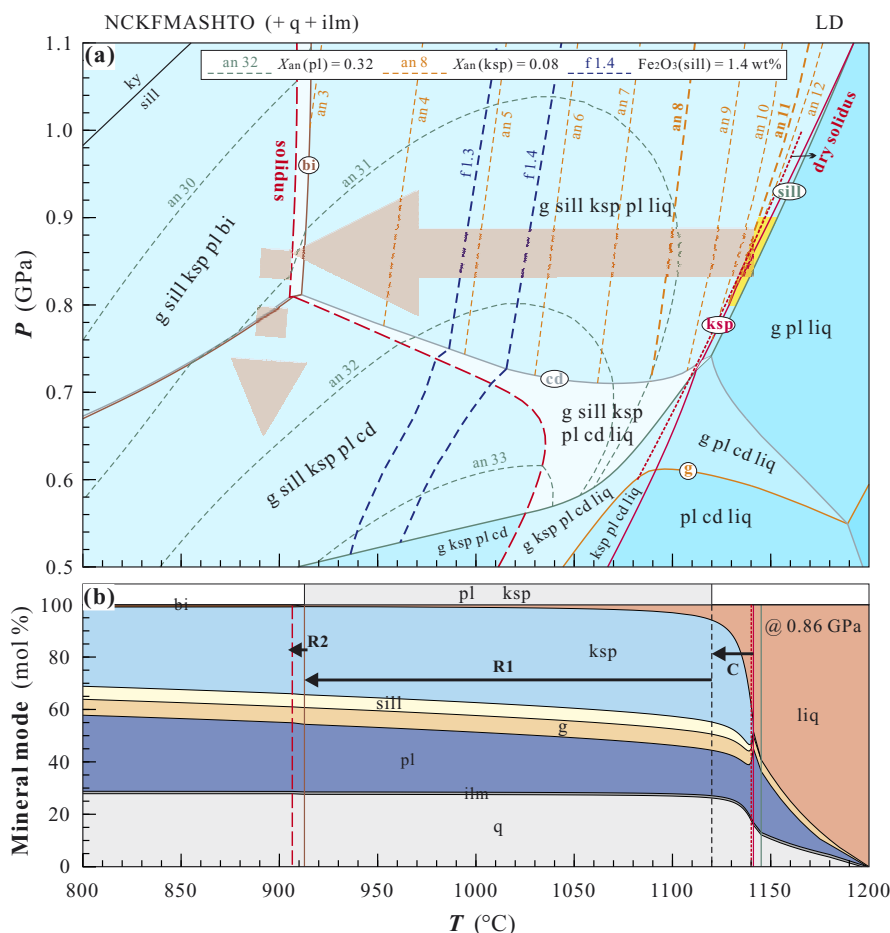
Fig. 12. (a) A *P–T* pseudosection with proposed peak conditions and *P–T* path. Others are the same as in Fig. 8a. (b) A *T*-Mode diagram showing the variation of mineral and melt mode, and the temperature ranges of melt crystallization (C) and crucial metamorphic reactions (R1 and R2) along the cooling path at 0·86 GPa.

1923 ± 24 to 1983 ± 28 Ma (Table 6), with a concordia age of 1945 ± 20 Ma (MSWD = 4·5) and a weighted mean age of 1943·9 ± 8·5 Ma (MSWD = 0·92; Fig. 14b, c). Six zircon grains included in sillimanite yield $^{207}Pb/^{206}Pb$ ages from 1918 ± 27–1978 ± 26 Ma (Table 6), with a concordia age of 1937 ± 22 Ma (MSWD = 0·95) and a weighted mean age of 1941 ± 15 Ma (MSWD = 0·97; Fig. 14b, c). However, six zircon grains included in biotite give $^{207}Pb/^{206}Pb$ ages from 1881 ± 10–1909 ± 8 Ma (Table 6), with an intercept age of 1904 ± 22 Ma (MSWD = 0·14) and a weighted mean age of 1900·4 ± 8·8 Ma (MSWD = 0·99; Fig. 14b, c). The $^{207}Pb/^{206}Pb$ ages of zircon grains included in perthite and sillimanite cannot be well differentiated from each other, and thus, the zircon ages are defined as two populations, ∼1·94 Ga and ∼1·90 Ga (Fig. 14c).

DISCUSSION

Metamorphic evolution

Petrologic analyses and phase equilibria modelling suggest that the three types of domains in the sapphirine-bearing granulite sample 17TPS underwent a uniform
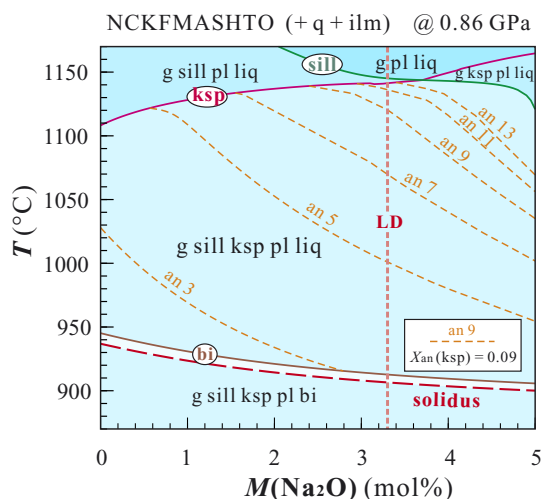
Fig. 13. A *T − M*(Na₂O) pseudosection calculated at 0·86 GPa based on the composition of LD, showing especially the variation of the *X*an(ksp) with the bulk-rock Na₂O contents. Others are the same as in Fig. 8a.

metamorphic evolution that involves three stages: peak temperature, post-peak cooling to the fluid-absent solidus and sub-solidus decompression.
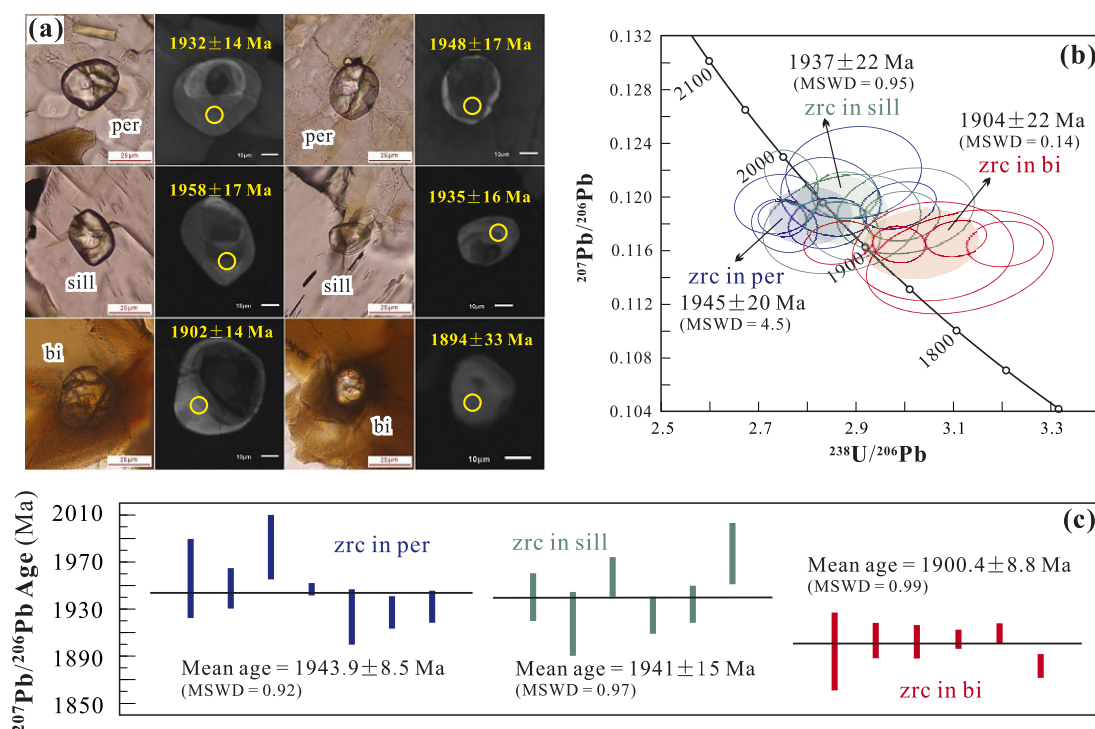
Fig. 14. (a) Photomicrographs showing zircon occurrence as inclusions in the labelled host minerals, and cathode-luminescence (CL) images showing zircon characters, $^{207}Pb/^{206}Pb$ ages and analytical sites. (b) A Tera–Wasserburg concordia diagram showing the age plots for the three groups of zircon that occur as inclusions in perthite, sillimanite and biotite. (c) The weighted mean $^{207}Pb/^{206}Pb$ ages for the three groups of zircon.

Table 6: Zircon U–Pb isotopic data and corrected ages

Host	U [ppm]	Th [ppm]	Th/U	Isotopic ratios				Corrected ages [Ma]			
				$^{207}Pb/^{206}Pb$	sd.%	$^{238}U/^{206}Pb$	sd.%	$^{207}Pb/^{206}Pb$	1σ sd.	$^{206}Pb/^{238}U$	1σ sd.
per	135	53	0·41	0·1259	1·63	2·827	2·4	1956	34	1941	40
	341	154	0·47	0·1204	0·94	2·733	2·1	1948	17	2008	36
	511	271	0·55	0·1242	1·51	2·887	3·2	1983	28	1913	53
	552	6	0·01	0·1195	0·27	2·985	1·8	1947	5	1862	28
	718	70	0·10	0·1179	1·31	2·753	1·7	1923	24	1997	28
	178	17	0·10	0·1180	0·72	2·841	1·8	1927	14	1944	31
	147	68	0·48	0·1171	0·53	2·752	1·2	1932	14	2001	21
sill	550	38	0·07	0·1192	1·12	3·000	3·1	1941	20	1854	50
	72	218	3·12	0·1196	0·81	2·867	1·7	1918	27	1925	29
	124	106	0·88	0·1205	0·60	2·875	1·5	1958	17	1923	25
	1127	106	0·10	0·1181	0·87	2·869	3·7	1925	16	1927	62
	143	92	0·66	0·1192	0·60	2·990	1·7	1935	16	1859	28
	73	76	1·07	0·1271	0·73	2·750	1·3	1978	26	1989	23
bi	104	75	0·74	0·1170	1·67	3·055	3·6	1894	33	1823	56
	172	154	0·93	0·1179	0·59	2·984	1·2	1903	15	1861	19
	178	92	0·54	0·1171	0·58	3·203	1·7	1902	14	1750	25
	225	63	0·29	0·1167	0·38	2·865	1·7	1904	8	1930	28
	399	52	0·14	0·1177	0·38	3·103	1·4	1909	8	1800	21
	273	77	0·29	0·1154	0·46	3·113	4·1	1881	10	1795	64

sd., standard deviation.

Peak temperature stage

The peak temperatures of UHT granulites from the classic outcrops at Tuguishan and Tianpishan are disputed to be 960–970 °C (Santosh *et al.*, 2009; Li & Wei, 2018), 1020–1050 °C (Jiao & Guo, 2011; Yang *et al.*, 2014) and >1100 °C (Liu *et al.*, 2011; Santosh *et al.*, 2012). This disagreement results mainly from the different approaches employed. The phase equilibria modelling results of the three compositional domains in the pelitic granulite sample at the Tianpishan outcrop suggest that the peak temperatures of the UHT metamorphism are over 1100 °C (or up to 1120–1140 °C) at pressures of 0·8–0·9 GPa, which are close to the dry solidi of ∼1130 °C calculated for the three domains (Fig. 15). These conditions are well consistent with the stability fields of the inferred K-feldspar-absent peak assemblages of sill-l +
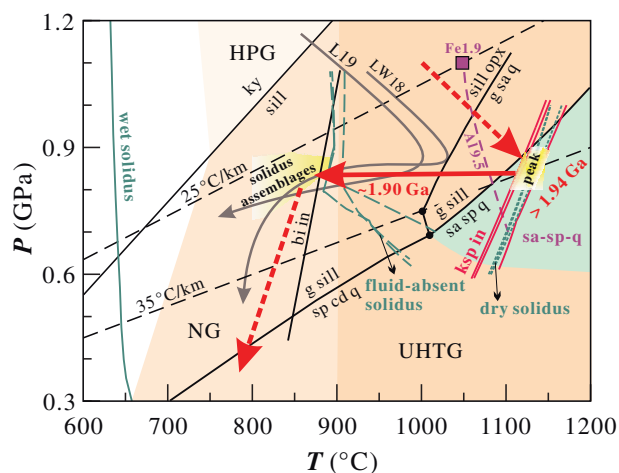
Fig. 15. A P–T–t path of UHT granulites from the Jining complex at the Tianpishan area (thick dashed and solid arrows) and its comparison with those in previous studies from Li & Wei (2018) at the Tuguiwula area (LW18) and Li *et al.* (2019) at the Hongshaba area (L19). Also shown are the experimental results for constraining (i) the stability range of the sa–sp–q assemblage, crucial metamorphic reactions (thin solid curves) and invariant points (solid dots) (Hensen, 1986; Kelsey *et al.*, 2004; Stevens *et al.*, 1997), (ii) the P–T condition for ferric sillimanite with 1.9 wt % Fe_2O_3 from Kawasaki *et al.* (2011) (the solid square labelled with Fe1.9); and (iii) the isopleth of the 9.5 wt % Al_2O_3 in orthopyroxene from Aranovich & Berman (1996) (the dashed curve labelled with Al9.5). The calculated dry solidi, fluid-absent solidi and K-feldspar-in (ksp in) lines in Figs 8a, 10a and 12a are presented with the corresponding labels. The granite wet solidus is cited from Johannes & Holtz (1996). The P–T ranges for the metamorphic facies of normal granulite (NG), ultrahigh-temperature granulite (UHTG) and high-pressure granulite (HPG) are cited from Brown (2007).

sa + sp + q in MD-s (Fig. 8a), sa + opx + q in MD-o (Fig. 10a) and the melt-dominated assemblage in LD (Fig. 12). The calculated stability range of the assemblage sa + sp + q matches the experimental constraints (Fig. 15; Hensen, 1986; Korhonen *et al.*, 2004; Kelsey *et al.*, 2004). The peak temperatures are also supported by the contours of mineral compositions, which includes the reintegrated Fe_2O_3 content ($2.1–2.3$ wt %) in sill-I in MD-s (Fig. 8a), the measured maximum Al^{IV} (0.22) in the orthopyroxene core in MD-o (Fig. 10a), and the reintegrated X_{an} ($0.08–0.11$) in K-feldspar (Fig. 12a) in LD. The calculated Fe_2O_3(sill) in MD-s and Al^{IV}(opx) in MD-o are in consistence with the previous constraints on Fe_2O_3(sill) of 1.9 wt % and Al^{IV}(opx) of 9.5 wt % (Fig. 15; Aranovich & Berman, 1996; Kawasaki *et al.*, 2011).

Post-peak cooling and sub-solidus decompression

The post-peak evolution is inferred to be nearly isobaric cooling (IBC) at $0.8–0.9$ GPa. The pressure is mainly indicated by the biotite- and orthopyroxene-bearing final assemblages in MD-s/o, where orthopyroxene is absent above ~ 0.9 GPa and the biotite is absent below

~ 0.8 GPa (Figs 8a, 10a). This pressure condition is consistent with the results from previous studies in the Jining complex (e.g. Jiao & Guo, 2011; Jiao *et al.*, 2013a; Li & Wei, 2016, 2018).

The post-peak cooling from the peak temperature to the fluid-absent solidus at $\sim 890\,°C$ involves various metamorphic reactions in the different domains. (1) The cooling evolution in MD-s involves the formation of K-feldspar followed by the sequential appearance of sill-II + g → opx → bi. This corresponds to the retrograde metamorphic reactions of R1 at $1025–1045\,°C$, R2 at $\sim 1010\,°C$, R3 at $900–1010\,°C$ and R4 at $\sim 900\,°C$ (Fig. 8b). Moreover, the temperature of R2 matches well with the values of $1000–1050\,°C$ from the experimental results (Bertrand *et al.*, 1991; Das *et al.*, 2003). In addition, the Fe_2O_3 contents in sill-II record the cooling from $\sim 1030\,°C$ to $\sim 900\,°C$ (Fig. 8a), and the ilm−tim pairs record re-equilibrated temperatures of $1003–1054\,°C$ using the Ti–Fe exchange geothermometer (Sauerzapf *et al.*, 2008). (2) The cooling evolution in MD-o involves the formation of K-feldspar followed by the sequential appearance of garnet and biotite, corresponding to the retrograde metamorphic reactions R1 at $900–1040\,°C$ and R2 at $\sim 900\,°C$ (Fig. 10b). The spectacular compositional zoning of orthopyroxene in MD-o with decreasing Al^{IV} from core to rim (Fig. 5c) records the cooling from $\sim 1120\,°C$ to $\sim 990\,°C$ (Fig. 10a). (3) The cooling evolution in LD involves the crystallization of segregated melts to produce K-feldspars at $1120–1140\,°C$, the exsolution of supra-solvus ternary feldspars through R1 at $910–1120\,°C$, and the growth of biotite at $\sim 910\,°C$ (Fig. 12b). The X_{an}(ksp) in LD records the initial cooling from $\sim 1140\,°C$ to $\sim 1100\,°C$, and the Fe_2O_3(sill) records temperatures of $990–1030\,°C$ (Fig. 12a).

The post-peak cooling evolution is followed by a decompression in sub-solidus conditions inferred from the occurrence of cordierite coronae around garnet, which yields much lower pressures as suggested by the cordierite stability ranges (Figs 8a, 10a, 12a) and cordierite-involved metamorphic reactions (Fig. 15).

Although there is no clear evidence to define what the pre-peak evolution of the UHT granulite is, the compression evolution from spinel-bearing assemblages to sapphirine-bearing ones proposed, such as in Santosh *et al.*, (2009), is not recommended because spinel and sapphirine are interpreted to coexist with each other as documented by the petrography in MD-s (Fig. 4c). Recent studies suggest that the pre-peak evolution of the UHT granulites is dominant of heating (Yang *et al.*, 2014; Lobjoie *et al.*, 2018) or decompression with heating (Li & Wei, 2016, 2018; Li *et al.*, 2019). The decompression combined with heating is supported by plagioclase zoning with core-to-rim elevated X_{an} (Li & Wei, 2016), ilmenite containing inclusions of rutile (Li & Wei, 2018) and garnet containing spinel inclusions in its rim domain (Li *et al.*, 2019). Thus, the UHT granulites at the Tianpishan area may have undergone a clockwise P–T evolution with the peak temperatures reaching up to $1120–1140\,°C$ (Fig. 15).

Timing of the UHT metamorphism

Most of the previous zircon U–Pb dating for UHT granulite samples from the Jining complex indicate a mean metamorphic age of 1·91–1·92 Ga (Santosh *et al.*, 2007*a*, 2013; Li & Wei, 2018; Lobjoie *et al.*, 2018; Li *et al.*, 2019), although a few younger ages of ∼1·88 Ga have also been reported (Yang *et al.*, 2014). Actually, all of these age analyses show wide and continuous spectrums on the concordia curve, for example, 1·79–1·96 Ga (Yang *et al.*, 2014) and 1·89–1·94 Ga (Li & Wei, 2018). Such a wide age spectrum can be ascribed to slow cooling of the UHT granulites (Li & Wei, 2016), and the geological meaning of the mean age could be ambiguous.

In-situ zircon dating in this study suggests two populations of metamorphic ages at ∼1·94 Ga and ∼1·90 Ga, respectively (Fig. 14c). The older age is defined from the zircon grains included in perthite and sillimanite which are inferred to be formed at the initial cooling stages (Fig. 8) when voluminous melts crystallized at very high temperatures (1010–1120 °C). The younger age is acquired from the zircon grains included in biotite that had crystallized at the late cooling stage close to the solidus. These results indicate that the UHT metamorphism in the Jining complex occurred at >1·94 Ga, consistent with the conclusions made by Li & Wei (2018), and the cooling under UHT conditions may have lasted over 40 Ma, comparable with the durations of slow and prolonged UHT metamorphism in terranes such as the Rogaland, Norway (Laurent *et al.*, 2018) and the Napier complex, Antarctica (Clark *et al.*, 2018). Moreover, this timing of cooling also complies with the exhumation age of ∼1·89 Ga that succeeds the UHT metamorphism, inferred from the garnetite in the Jining complex (Jiao *et al.*, 2013*a*, 2013*b*).

Mineral compositional typomorphism for UHT metamorphism

Al in orthopyroxene

Al in orthopyroxene (Al-in-opx) is one of the most widely used thermometers to estimate peak temperatures of granulites (e.g. Harley, 1998*b*; Hollis & Harley, 2003; Pattison *et al.*, 2003), especially, almost all the extreme UHT conditions over 1100 °C were constrained by Al-in-opx (e.g. Harley & Motoyoshi, 2000; Moraes *et al.*, 2002; Sajeev & Osanai, 2004). This is because the Al diffusivity is slow as a result of its incorporation via Tschermak ion exchange in the framework of mineral lattices (e.g. Kelsey & Hand, 2015). Harley (2008) proposed that > 8 wt % of Al_2O_3 in orthopyroxene can be an indicator of UHT conditions, whilst Kelsey (2008) presented that y(opx) (= $Al^{VI} \approx Al^{IV}$) > 0·14 (Al_2O_3 > 6 wt %) in normal pelitic rocks, and y(opx) > 0·19 (Al_2O_3 > 8 wt %) in Fe-rich pelitic rocks, can indicate UHT conditions.

As the Al^{VI} in orthopyroxene may easily vary due to the Al^{VI}–Fe^{3+} diffusion between minerals and the change in oxygen fugacity during cooling, consequently increasing uncertainties for temperature estimation, the Al^{IV} in orthopyroxene was employed as temperature indicator in this study. The phase equilibria modelling results presented above suggest that the Al-in-opx thermometer mainly depends on the variation in bulk rock composition and mineral assemblage. For instance, the *P*–*T* pseudosection (Fig. 10a) shows that the Al^{IV}(opx) is dominantly temperature-dependent in the lower-pressure garnet-absent and sapphirine-present fields and is considerably influenced by pressure in the higher-pressure garnet- and sapphirine-present fields, while it is mostly pressure-dependent in the sapphirine-absent field (opx−ksp−g−liq). The *T*–A/AFM pseudosection (Fig. 11a) indicates that the Al-in-opx can be used as a good thermometer only in the Al-saturated assemblages (A/AFM > 0·18) where an Al-rich phase such as sapphirine or sillimanite is present, while in the Al-undersaturated assemblages, the Al^{IV}(opx) depends only on the bulk-rock Al_2O_3 content and has nothing to do with temperature. The T –X_{Mg} pseudosection (Fig. 11b) shows that the Al^{IV}(opx) increases as temperature rises but varies considerably as the bulk-rock X_{Mg} changes. For a UHT indicating orthopyroxene, the minimum Al^{IV}(opx) value of 0·14 is valid for the bulk-rock X_{Mg} range of 0·7–0·8, and it will decrease in more Mg-rich and Fe-rich rocks. In the present study, the maximum Al_2O_3 of 9·5 wt % (Al^{IV} = 0·22) from a coarse-grained orthopyroxene core yields a peak temperature up to 1120 °C in the assemblage with opx + sa for the bulk-rock A/AFM = 0·21 and X_{Mg} = 0·75. For the same Al_2O_3 content, the temperature estimates may somewhat increase or decrease with changes in bulk-rock composition. In the assemblage with opx + g for the bulk-rock X_{Mg} = 0·6, the isopleth of Al^{IV} = 0·22 can yield a lower temperature of ∼1075 °C (Fig. 11b), which is basically consistent with the result obtained using the opx−g Al-solubility thermometer (Harley & Green, 1982), assuming that the orthopyroxene core equilibrated with garnet. For the experimental syntheses in the MgO–Al_2O_3–SiO_2 system, orthopyroxene with 9·5 wt % Al_2O_3 can even stabilize at temperatures over 1200 °C (Arima & Onuma, 1977).

Fe_2O_3 in sillimanite

Natural Al_2SiO_5-group minerals commonly occur as solid solutions with Fe^{3+} and Mn^{3+} substituting for Al, especially under low-*P*–high-*T* or highly oxidized conditions (Kramm, 1979; Grew, 1980; Grambling & Williams, 1985). For example, sillimanite with various Fe_2O_3 contents has been reported in gneissic xenoliths (Grew, 1980; Sassi *et al.*, 2004) and high-grade metamorphic rocks (Grew, 1980; Grambling & Williams, 1985). Calculations indicate that decreasing pressure or increasing temperature can increase Fe_2O_3 in sillimanite (Grambling & Williams, 1985). Statistics of both natural and synthetic samples suggest an almost linear relationship between the Fe_2O_3 in sillimanite and temperature (e.g. Sengupta *et al.*, 1991; Sarkar *et al.*, 2003; Sassi *et al.*, 2004; Santosh *et al.*, 2007*b*; Kawasaki *et al.*, 2011; Shimizu *et al.*, 2013). On the basis of this linear

relation, we explored a symmetric α–X model aided with DQF parameters to simulate the mixing of Fe_2O_3 in sillimanite. The phase equilibria modelling results involving this new α–X model for ferric sillimanite as shown in Fig. 8a suggest that the isopleths of Fe_2O_3(sill) show steep slopes in most assemblages, being a good temperature indicator, and the Fe_2O_3 content from 1·3–2·5 wt % indicates a temperature increase from ~900 to ~1180 °C at 0·8–0·9 GPa in MD-s, which is in accordance with the statistical data from the previous studies (e.g. Sengupta *et al.*, 1991; Sarkar *et al.*, 2003; Kawasaki *et al.*, 2011). However, the isopleths of Fe_2O_3(sill) in LD has relatively lower values than those in MD-s at the same temperature (Fig. 12a), which may be ascribed to the different bulk-rock X_{Fe}^{3+} between the two domains (Fig. 9; Table 5). The $T - X_{Fe}^{3+}$ pseudosection (Fig. 9) also shows that the bulk-rock X_{Fe}^{3+} takes relatively slight effects on the Fe_2O_3(sill) isopleths in oxidized situations ($X_{Fe}^{3+} > $~0·4). As a result, the Fe_2O_3(sill) can be appropriately used as a temperature indicator in oxidized UHT metapelites such as those in the Tianpishan area (Li & Wei, 2018), but should be treated with caution in reduced rocks.

Although Fe_2O_3 in sillimanite can be easily absorbed by neighbouring Ti–Fe oxides (e.g. Grew, 1980), the coarse-grained sillimanite can preserve considerable Fe_2O_3 in the core, or exhibit hematite exsolutions like that in MD-s (Fig. 4a). The reintegrated Fe_2O_3 of 2·1–2·3 wt % in sill-l yields consistent peak temperature conditions with those constrained by the Al^{IV}(opx) and X_{an}(ksp) isopleths. On the other hand, the exsolution-absent sillimanite that contains the maximum Fe_2O_3 of 1·8 wt % yields temperatures of 1020–1040 °C (Fig. 8a). As a result, sillimanite with exsolved hematite may suggest temperature conditions >1000 °C. This corresponds to the reports that sillimanite with exsolved hematite occurs only in UHT rocks above 1000 °C (Sarkar *et al.*, 2003; Korhonen & Stout, 2004).

In addition, the calculated phase relations with the involvement of ferric sillimanite are somewhat different from those in Li & Wei (2018). For instance, the stability of the sill + opx assemblage is extended, while the stability of the sa + q assemblage is reduced (Fig. 8a), well consistent with the experimental results shown in Fig. 15 (Hensen, 1986).

Anorthite in K-feldspar

UHT metapelites commonly contain perthite formed from supra-solvus ternary high-Ca–Na K-feldspar (e.g. Kelsey & Hand, 2015), and the reintegrated ternary feldspar compositions were widely used to retrieve peak temperatures of UHT granulites (e.g. Hokada, 2001; Pilugin *et al.*, 2009; Jiao & Guo, 2011). However, the temperature estimates may vary considerably due to the application of different mixing models of feldspar (e.g. Fuhrman & Lindsley, 1988; Elkins & Grove, 1990). Particularly, K-feldspars with different compositional domains yield different temperatures using the

graphical thermometry as shown in Fig. 5d. For example, perthite from MD-s/o and LD in the present study was reintegrated to show X_{an}(ksp) of 0·05–0·06 and 0·08–0·11, respectively, which yield temperatures of 1000 °C and slightly <1100 °C based on the model of Elkins & Grove (1990), but much lower temperatures of ~900 °C and ~1000 °C based on the model of Fuhrman & Lindsley (1988) in Fig. 5d. However, the X_{an}(ksp) isopleths with these different values yield roughly similar temperatures of 1100 ± 30 °C from the calculated pseudosections (Figs 8a, 10a, 12a), approximate to the results defined from the model of Elkins & Grove (1990) for the higher X_{an}(ksp) values of 0·08–0·11. These cases suggest that the X_{an}(ksp) thermometer can be influenced by the diversity of bulk-rock composition. The phase relations in Fig. 13 suggest that the X_{an}(ksp) depends considerably on the bulk-rock Na_2O content besides temperature. For instance, K-feldspar in Na_2O-richer rocks can hold more CaO at the same temperature, or vice versa as a certain X_{an}(ksp) value can give higher temperature estimates in Na_2O-lower rocks. This is because K-feldspar in Na_2O-rich rocks (such as LD with 3·29 mol % Na_2O) may contain more Na_2O than that in Na_2O-lower rocks (such as MD-s/o with 0·52–0·68 mol % Na_2O) (Tables 3–5), and the NaSi–CaAl exchange is much easier to occur in feldspar than the KSi–CaAl exchange (e.g. Fuhrman & Lindsley, 1988). Hence, the An–Ab–Or graphical thermometry should be used carefully in view of the diverse bulk-rock compositions and activity models.

Geologic implications

The UHT metamorphism at the Tianpishan area was revealed to yield peak temperatures up to 1120–1140 °C (at 0·8–0·9 GPa), implying a geothermal gradient of 35 °C/km (Fig. 15). As the peak temperatures are close to the calculated dry solidus of ~1130 °C (at 0·8–0·9 GPa) for the studied rock (Fig. 15), the crustal rocks may have experienced extensive diatexis as shown in Fig 2a, where the studied restite-dominated granulites occur only as melanocratic schlieren in melt-dominated leucosomes, and the stratigraphic sequences are totally dismembered. The extracted melts with peritectic minerals formed the massive garnet-bearing granites in the region (Fig. 1c). The UHT rocks with extreme peak temperatures above 1100 °C should limitedly occur at the Tuguiwula, Xuwujia and Tianpishan areas (Fig. 1c; Liu *et al.*, 2011; Santosh *et al.*, 2012; Wang *et al.*, 2019), and the peak temperatures decline to about 950–1050 °C at the Hongsigou, Zhaojiayao, Xumayao, Helinger and Hongshaba areas (Fig. 1c; Liu *et al.*, 2012; Zhang *et al.*, 2012; Yang *et al.*, 2014; Li & Wei, 2016; Li *et al.*, 2019).

In-situ SHRIMP zircon U–Pb dating and phase equilibria modelling indicate that the UHT granulites together with voluminous garnet-bearing granites may have experienced a slow cooling history over 40 Ma from >1·94 to ~1·90 Ga at an 0·8–0·9 GPa crustal level. Such a long-term stagnation of highly melted crustal rocks at a

deep level can be attributed to the following facts: (1) the highly melted crustal lithosome like that shown in Fig. 2a and the garnet-bearing granites with peritectic garnet up to 25% (Wang *et al.*, 2018) are calculated to share similar densities of 2·73– 2·71 g/cm^3, even slightly greater than the average density of 2·7 g/cm^3 for continental crust (Jamieson & Beaumont, 2011); and (2) the melts with low water but abundant suspended restites and peritectic minerals may have a much higher viscosity according to the Einstein–Roscoe equation (Roscoe, 1952; Shaw, 1972), making the melts stagnant but not extractable. As a consequence, both the granitic magmas and the highly melted crustal lithosome did not ascend upward, but underwent parautochthonous crystallization and isobaric cooling.

The tectonic regime for the UHT metamorphism in the Jining complex is controversially discussed, as opinions vary from a plume event (e.g. Santosh *et al.*, 2008), ridge subduction (e.g. Peng *et al.*, 2010; Guo *et al.*, 2012; Santosh *et al.*, 2012), to post-collision mantle upwelling together with mafic magma emplacement (e.g. Zhao, 2009; Li & Wei, 2018). Previous studies suggest that the UHT metamorphism in the Jining complex may have been preceded by an orogenic crustal thickening event that occurred at 1·98–1·96 Ga (Li *et al.*, 2011; Yin *et al.*, 2011). This is supported by a high-pressure granulite facies metamorphism with clockwise *P–T* path (e.g. Zhou *et al.*, 2010) and anatectic leucogranite (Guo *et al.*, 1999). Following the post-orogenic crustal extension at ∼1·95 Ga (e.g. Dan *et al.*, 2012; Wan *et al.*, 2013), the UHT metamorphism was considered to occur based on its clockwise *P–T* paths (e.g. Li & Wei, 2018) and the zircon dates in this study. It may be accompanied with gabbronorite emplacement at ∼1·93 Ga (Peng *et al.*, 2010) and garnet granite formation at 1·92–1·90 Ga (Zhong *et al.*, 2007; Wang *et al.*, 2018; Shi *et al.*, 2018). Moreover, the gabbronorites were estimated to have intrusive temperatures up to 1400 °C, with an anomalously high mantle potential temperature of 1550 °C, consistent with a plume activity (Peng *et al.*, 2010; Gibson *et al.*, 2006). Therefore, we prefer that the extreme UHT metamorphism in the Jining complex may have been triggered by the advective heating of intraplated hyperthermal mafic magma together with a plume-related hot mantle upwelling (e.g. Wang *et al.*, 2019), following an orogenic crustal thickening event. This is consistent with the limited occurrences of UHT granulites with peak temperatures above 1100 °C close to mafic intrusions.

REFERENCES

Aranovich, L. Y. & Berman, R. G. (1996). Optimized standard state and solution properties of minerals ll. Comparisons, predictions, and applications. *Contributions to Mineralogy and Petrology* **126**, 25–37.

Arima, M. & Onuma, K. (1977). The solubility of alumina in enstatite and the phase equilibria in the join MgSiO$_3$–MgAl$_2$SiO$_6$ at 10–25 kbar. *Contributions to Mineralogy and Petrology* **61**, 251–265.

Bertrand, P., Ellis, D. J. & Green, D. H. (1991). The stability of sapphirine-quartz and hypersthene-sillimanite-quartz assemblages assemblages: an experimental investigation in the system FeO-MgO-Al$_2$O$_3$-SiO$_2$ under H$_2$O and CO$_2$ conditions. *Contributions to Mineralogy and Petrology* **108**, 55–71.

Brandt, S., Schenk, V., Raith, M., Appel, P., Gerdes, A. & Srikantappa, C. (2011). Late Neoproterozoic P-T evolution of HP-UHT granulites from the Palni Hills (South India): New constraints from phase diagram modelling, LA-ICP-MS zircon dating and in-situ EMP monazite dating. *Journal of Petrology* **52**, 1813–1856.

Brown, M. (2006). Duality of thermal regimes is the distinctive characteristic of plate tectonics since the Neoarchaean. *Geology* **34**, 961–964.

Brown, M., Ernst, W. G. & Rumble, D. (2007). Metamorphic conditions in orogenic belts: a record of secular change. *International Geology Review* **49**, 193–234.

Burg, J. P. & Gerya, T. V. (2005). The role of viscous heating in Barrovian metamorphism of collisional orogens: thermomechanical models and application to the Lepontine Dome in the Central Alps. *Journal of Metamorphic Geology* **23**, 75–95.

Cai, J., Liu, F. L., Liu, P. H. & Shi, J. R. (2014). Metamorphic P-T conditions and U–Pb dating of the sillimanite–cordierite–garnet paragneisses in Sanchakou, Jining area, Inner Mongolia. *Acta Petrologica Sinica* **30**, 472–490.

Cai, J., Liu, F. L., Liu, P. H., Wang, F. & Shi, J. R. (2015). Geochronology of the Paleoproterozoic khondalite rocks from the Wulashan-Daqingshan area, the Khondalite belt. *Acta Petrologica Sinica* **31**, 3081–3106.

Charlu, T. V., Newton, R. C. & Kleppa, O. J. (1975). Enthalpies of solution at 970 K of compounds in the system MgO-Al$_2$O$_3$-SiO$_2$ by high temperature solution calorimetry. *Geochimica et Cosmochimica Acta* **39**, 1487–1497.

Clark, C., Fitzsimons, I. C. W., Healy, D. & Harley, S. L. (2011). How does the continental crust get really hot. *Elements* **7**, 235–240.

Clark, C., Taylor, R. J. M., Kylander-Clark, A. R. C. & Hacker, B. R. (2018). Prolonged (>100 Ma) ultrahigh temperature metamorphism in the Napier Complex, East Antarctica: a petrochronological investigation of Earth's hottest crust. *Journal of Metamorphic Geology* **36**, 1117–1139.

Collins, W. J. (2002). Hot orogens, tectonic switching, and creation of continental crust. *Geology* **30**, 535–538.

Condie, K. C., Boryta, M. D., Liu, J. Z. & Qian, X. L. (1992). The origin of khondalites: Geochemical evidence from the

Archean to Early Proterozoic granulite belt in the North China Craton. *Precambrian Research* **59**, 207–223.

Corfu, F., Hanchar, J. M., Hoskin, P. W. & Kinny, P. (2003). Atlas of zircon textures. *Reviews in Mineralogy and Geochemistry* **53**, 469–500.

Currie, C. A. & Hyndman, R. D. (2006). The thermal structure of subduction zone back arcs. *Journal of Geophysical Research* **111**, 1–22.

Dan, W., Li, X. H., Guo, J. H., Liu, Y. & Wang, X. C. (2012). Integrated in situ zircon U-Pb age and Hf–O isotopes for the Helanshan khondalites in North China Craton: juvenile crustal materials deposited in active or passive continental margin? *Precambrian Research* **222-223**, 143–158.

Das, K., Dasgupta, S. & Miura, H. (2003). An experimentally constrained petrogenetic grid in the silica-saturated portion of the system KFMASH at high temperatures and pressures. *Journal of Petrology* **44**, 1055–1075.

Dong, C., Liu, D., Li, J., Wang, Y., Zhou, H., Li, C., Yang, Y. & Xie, L. (2007). Palaeoproterozoic Khondalite Belt in the western North China Craton: New evidence from SHRIMP dating and Hf isotope composition of zircons from metamorphic rocks in the Bayan Ul-Helan Mountains area. *Chinese Science Bulletin* **52**, 2984–2994.

Dong, C. Y., Wan, Y. S., Xu, Z. Y., Liu, D. Y., Yang, Z. S., Ma, M. Z. & Xie, H. Q. (2013). SHRIMP zircon U-Pb dating of late Paleoproterozoic kondalites in the Daqing Mountains area on the North China Craton. *Science China Earth Sciences* **56**, 115–125.

Dong, J., Wei, C. J., Clarke, G. L. & Zhang, J. X. (2018). Metamorphic evolution during deep subduction and exhumation of continental crust: insights from felsic granulites in South Altyn Tagh. *Journal of Petrology* **59**, 1965–1990.

Dong, J., Wei, C. J. & Zhang, J. (2019). Ultrahigh temperature metamorphism of mafic granulites from South Altyn Orogen, West China: a result from the rapid exhumation of deeply subducted continental crust. *Journal of Metamorphic Geology* **37**, 315–338.

Elkins, L. T. & Grove, T. L. (1990). Ternary feldspar experiments and thermodynamic models. *American Mineralogist* **75**, 544–559.

Ellis, D. J., Sheraton, J. W., England, R. N. & Dallwitz, W. B. (1980). Osumilite-sapphirine-quartz granulites from Enderby Land Antarctica—mineral assemblages and reactions. *Contributions to Mineralogy and Petrology* **72**, 123–143.

Fleet, M. & Arima, M. (1985). Oriented hematite inclusions in sillimanite. *American Mineralogist* **14**, 194–202.

Fuhrman, M. L. & Lindsley, D. H. (1988). Ternary-feldspar modeling and thermometry. *American Mineralogist* **73**, 201–215.

Gibson, S. A., Thompson, R. N. & Day, J. A. (2006). Timescales and mechanisms of plume–lithosphere interactions: $^{40}Ar/^{39}Ar$ geochronology and geochemistry of alkaline igneous rocks from the Parana–Etendeka large igneous province. *Earth and Planetary Science Letters* **251**, 1–17.

Grambling, J. A. & Williams, M. L. (1985). The effects of Fe^{3+} and Mn^{3+} on aluminum silicate phase relations in north-central New Mexico, USA. *Journal of Petrology* **26**, 324–354.

Grew, E. S. (1980). Sillimanite and ilmenite from high-grade metamorphic rocks of Antarctica and other areas. *Journal of Petrology* **21**, 39–68.

Guo, J. H., Chen, Y., Peng, P., Liu, F., Chen, L. & Zhang, L. Q. (2006). Sapphirine granulite from Daqingshan area, Inner Modolia - 1.85Ga ultrahigh temperature (UHT) metamorphism. *Proceedings of National Conference on Petrology and Geodynamics in China (Nanjing)*, 215–218.

Guo, J. H., Peng, P., Chen, Y., Jiao, S. J. & Windley, B. F. (2012). UHT sapphirine granulite metamorphism at 1.93–1.92 Ga caused by gabbronorite intrusions: implications for tectonic evolution of the northern margin of the North China Craton. *Precambrian Research* **222-223**, 124–142.

Guo, J. H., Shi, X., Bian, A., Xu, R., Zhai, M. G. & Li, Y. (1999). Pb isotopic composition of feldspar and U–Pb age of zircon from early Proterozoic granite in Sanggan area, North China Craton: metamorphism, crustal melting and tectono-thermal event. *Acta Petrologica Sinica* **15**, 199–207.

Guo, J. H., Wang, S. S., Sang, H. Q. & Zhai, M. G. (2001). $^{40}Ar–^{39}Ar$ age spectra of garnet porphyroblast: implications for metamorphic age of high-pressure granulite in the North China Craton. *Acta Petrologica Sinica* **17**, 436–442.

Guo, J. H., Zhai, M. G. & Xu, R. H. (2002). The ages of large-scale granulite facies metamorphism in Sanggan area, North China: Zircon U-Pb chronology. *Science China Earth Sciences* **32**, 10–18.

Harley, S. L. (1998a). On the Occurrence and Characterisation of Ultrahigh-Temperature (UHT) Crustal Metamorphism. In: Treloar, P. J. & O'Brien, P. (eds) *What Controls Metamorphism and Metamorphic Reactions*. London: Geological Society of London, Special Publication **138**, 75–101.

Harley, S. L. (1998b). Ultrahigh temperature granulite metamorphism (1050 °C, 12 kbar) and decompression in garnet (Mg70)-orthopyroxene-sillimanite gneisses from the Rauer group. *Journal of Metamorphic Geology* **16**, 541–562.

Harley, S. L. (2004). Extending our understanding of ultrahigh temperature crustal metamorphism. *Journal of Mineralogical and Petrological Sciences* **99**, 140–158.

Harley, S. L. (2008). Refining the P-T records of UHT crustal metamorphism. *Journal of Metamorphic Geology* **26**, 125–154.

Harley, S. L. (2016). A matter of time: the importance of the duration of UHT metamorphism. *Journal of Mineralogical and Petrological Sciences* **111**, 50–72.

Harley, S. L. & Green, D. H. (1982). Garnet–orthopyroxene barometry for granulites and peridotites. *Nature* **300**, 697–701.

Harley, S. L. & Motoyoshi, Y. (2000). Al zoning in orthopyroxene in a sapphirine quartzite: evidence for >1120 °C UHT metamorphism in the Napier complex, Antarctica, and implications for the entropy of sapphirine. *Contributions to Mineralogy and Petrology* **138**, 293–307.

Hensen, B. J. (1986). Theoretical phase relations involving cordierite and garnet revisited: the influence of oxygen fugacity on the stability of sapphirine and spinel in the system Mg-Fe-Al-Si-O. *Contributions to Mineralogy and Petrology* **92**, 362–367.

Hokada, T. (2001). Feldspar thermometry in ultrahigh-temperature metamorphic rocks: Evidence of crustal metamorphism attaining ~1100 °C in the Archean Napier Complex, East Antarctica. *American Mineralogist* **86**, 932–938.

Holland, T. J. B. & Powell, R. (2011). An improved and extended internally-consistent thermodynamic dataset for phases of petrological interest, involving a new equation of state for solids. *Journal of Metamorphic Geology* **29**, 333–383.

Hollis, J. A. & Harley, S. L. (2003). Alumina solubility in orthopyroxene coexisting with sapphirine and quartz. *Contributions to Mineralogy and Petrology* **144**, 473–483.

Hyndman, R. D., Currie, C. A. & Mazzotti, S. P. (2005). Subduction zone back-arcs, mobile belts, and orogenic heat. *GSA Today* **15**, 4–10.

Ireland, T. R. & Williams, I. S. (2003). Considerations in zircon geochronology by SIMS. *Reviews in Mineralogy and Geochemistry* **53**, 215–241.

Jamieson, R. A. & Beaumont, C. (2011). Coeval thrusting and extension during lower crustal ductile flow-implications for

exhumation of high-grade metamorphic rocks. *Journal of Metamorphic Geology* **29**, 33–51.

Jiao, S. J. & Guo, J. H. (2011). Application of the two-feldspar geothermometer to ultrahigh-temperature (UHT) rocks in the Khondalite belt, North China craton and its implications. *American Mineralogist* **96**, 250–260.

Jiao, S. J., Guo, J. H., Harley, S. L. & Peng, P. (2013b). Geochronology and trace element geochemistry of zircon, monazite and garnet from the garnetite and/or associated other high-grade rocks: Implications for Palaeoproterozoic tectonothermal evolution of the Khondalite Belt, North China Craton. *Precambrian Research* **237**, 78–100.

Jiao, S. J., Guo, J. H., Harley, S. L. & Windley, B. F. (2013a). New constraints from garnetite on the P-T path of the Khondalite Belt: implications for the tectonic evolution of the North China Craton. *Journal of Petrology* **54**, 1725–1758.

Johannes, W. & Holtz, F. (1996). Petrogenesis and experimental petrology of granitic rocks. In: El Goresy, A., von Engelhardt, W. & Hahn, T. (eds) *Minerals and Rocks*. Berlin: Springer Verlag.

Kawasaki, T., Osanai, Y. & Ishizuka, H. (2011). An experimental study on Fe_2O_3 solubility in sillimanite to calibrate Fe-in-sillimanite geothermobarometer for ultrahigh-temperature granulites. *Proceedings of the 11th International Symposium on Antarctic Earth Sciences*, Edinburgh, Scotland.

Kelsey, D. E. (2008). On ultrahigh-temperature crustal metamorphism. *Gondwana Research* **13**, 1–29.

Kelsey, D. E. & Hand, M. (2015). On ultrahigh temperature crustal metamorphism: Phase equilibria, trace element thermometry, bulk composition, heat sources, timescales and tectonic settings. *Geoscience Frontiers* **6**, 311–356.

Kelsey, D. E., White, R. W., Holland, T. J. B. & Powell, R. (2004). Calculated phase equilibria in K_2O-FeO-MgO-Al_2O_3-SiO_2-H_2O for sapphirine-quartz-bearing mineral assemblages. *Journal of Metamorphic Geology* **22**, 559–578.

Korhonen, F. J., Clark, C. W., Brown, M. & Taylor, R. (2014). Taking the temperature of Earth's hottest crust. *Earth and Planetary Science Letters* **408**, 341–354.

Korhonen, F. J., Powell, R. & Stout, J. H. (2012). Stability of sapphirine + quartz in the oxidized rocks of the Wilson Lake terrane, Labrador: calculated equilibria in NCKFMASHTO. *Journal of Metamorphic Geology* **30**, 21–36.

Korhonen, F. J., Saw, A. K., Clark, C., Brown, M. & Bhattacharya, S. (2011). New constraints on UHT metamorphism in the Eastern Ghats Province through the application of phase equilibria modelling and in situ geochronology. *Gondwana Research* **20**, 764–781.

Korhonen, F. J., Stout, J. H., (2004). Low-Variance Sapphirine-Bearing Assemblages from Wilson Lake, Grenville Province of Labrador. In: Tollo, R. P., Corriveau, L., McLelland, J. & Bartholomew, M. J. (eds) *Proterozoic Tectonic Evolution of the Grenville Orogen in North America.* Boulder, Colorado: Geological Society of America **197**, pp. 81–103.

Kramm, U. (1979). Kanonaite-rich viridines from the Venn-Stavelot massif, Belgian Ardennes. *Contributions to Mineralogy and Petrology* **69**, 387–395.

Kriegsman, L. M. (2001). Partial melting, partial melt extraction and partial back reaction in anatectic migmatites. *Lithos* **56**, 75–96.

Laurent, A. T., Bingen, B., Duchene, S., Whitehouse, M. J., Seydoux-Guillaume, A. M. & Bosse, V. (2018). Decoding a protracted zircon geochronological record in ultrahigh temperature granulite, and persistence of partial melting in the crust, Rogaland, Norway. *Contributions to Mineralogy and Petrology* **173**, 29.

Lee, B. C., Oh, C. W., Kim, T. S. & Yi, K. (2016). The metamorphic evolution from ultrahigh-temperature to amphibolite facies metamorphism in the Odaesan area after the collision between the North and South China Cratons in the Korean Peninsula. *Lithos* **256-257**, 109–131.

Li, X., Zhang, L., Wei, C., Slabunov, A. I. & Bader, T. (2018). Ultrahigh-temperature metamorphism in the Tuguiwula area, Khondalite belt, North China Craton. *Journal of Metamorphic Geology* **36**, 1–21.

Li, X. L., Zhang, L. F., Wei, C. J., Slabunov, A. I. & Bader, T. (2018). Quartz and orthopyroxene exsolution lamellae in clinopyroxene and the metamorphic *P–T* path of Belomorian eclogites. *Journal of Metamorphic Geology* **36**, 1–12.

Li, X. P., Yang, Z. Y., Zhao, G. C., Grapes, R. & Guo, J. H. (2011). Geochronology of khondalite-series rocks of the Jining Complex: confirmation of depositional age and tectonometamorphic evolution of the North China Craton. *International Geology Review* **53**, 1194–1211.

Li, X. W. & Wei, C. J. (2018). Ultrahigh-temperature metamorphism in the Tuguiwula area, Khondalite belt, North China Craton. Journal of Metamorphic Geology **36**, 1–21.

Li, X. W. & Wei, C. J. (2016). Phase equilibria modelling and zircon age dating of pelitic granulites in Zhaojiayao, from the Jining Group of the Khondalite Belt, North China Craton. *Journal of Metamorphic Geology* **34**, 595–615.

Li, X. W., White, R. W. & Wei, C. J. (2019). Can we extract ultrahigh-temperature conditions from Fe-rich metapelites? An example from the Khondalite Belt, North China Craton. *Lithos* **328-329**, 228–243.

Liu, P., Liu, F., Liu, C., Liu, J., Wang, F., Xiao, L., Cai, J. & Shi, J. (2014). Multiple mafic magmatic and high-grade metamorphic events revealed by zircons from meta-mafic rocks in the Daqingshan-Wulashan Complex of the Khondalite Belt, North China Craton. *Precambrian Research* **246**, 334–357.

Liu, S. J. & Li, J. H. (2007). Review of ultrahigh-temperature (UHT) metamorphism study: a case from North China Craton. *Geoscience Frontiers* **14**, 131–137.

Liu, S. J., Tsunogae, T., Li, W. S., Shimizu, H., Santosh, M., Wan, Y. S. & Li, J. H. (2012). Paleoproterozoic granulites from Heling'er: implications for regional ultrahigh-temperature metamorphism in the North China Craton. *Lithos* **148**, 54–70.

Liu, S. J., Xiang, B., Li, J. H. & Santosh, M. (2011). Retrograde metamorphism of ultrahigh-temperature granulites from the Khondalite belt in Inner Mongolia, North China Craton: evidence from aluminous orthopyroxenes. *Geological Journal* **46**, 263–275.

Lobjoie, C., Lin, W., Trap, P., Goncalves, P., Li, Q., Marquer, D., Bruguier, O. & Devoir, A. (2018). Ultra-high temperature metamorphism recorded in Fe-rich olivine-bearing migmatite from the Khondalite belt, North China Craton. *Journal of Metamorphic Geology* **36**, 343–368.

Lu, L. Z., Jin, S. Q., Xu, X. C. & Liu, F. L. (1992). *The Genesis of Early Precambrian Khondalite Series in Southeastern Inner Mongolia and Its Potential Mineral Resources*. Changchun: Jilin Scientific and Technical Publishing House (in Chinese).

Lu, L. Z., Xu, X. C. & Liu, F. L. (1996). *Early Precambrian Khondalite Series in North China*. Changchun: Changchun Publishing House (in Chinese).

Ludwig, K. R. (2003). *ISOPLOT 3.00: A Geochronological Toolkit for Microsoft Excel*. Berkeley, California: Berkeley Geochronology Center, pp. 39.

Macdonald, J., Wheeler, J., Goodenough, K., Harley, S. L., Crowley, Q. & Mariani, E. (2011). Combined SIMS U-Pb ages and Ti-in-zircon geothermometry fingerprints long deep

crustal residence in the Archaean. *Mineralogical Magazine* **75**, 1377.

Mahar, E. M., Baker, J. M., Powell, R., Holland, T. J. B. & Howell, N. (1997). The effect of Mn on mineral stability in metapelites. *Journal of Metamorphic Geology* **15**, 223–238.

Majzlan, J., Navrotsky, A. & Evans, B. J. (2002). Thermodynamics and crystal chemistry of the hematite–corundum solid solution and the $FeAlO_3$ phase. *Physics and Chemistry of Minerals* **29**, 515–526.

Moraes, R., Brown, M., Fuck, R. A., Camargo, M. A. & Lima, T. M. (2002). Characterization and P-T evolution of melt-bearing ultrahigh-temperature granulites: an example from the Anapolis-Itaucu Complex of the Brasilia fold belt. *Journal of Petrology* **43**, 1673–1705.

Osanai, Y., Hamamoto, T., Maishima, O. & Kagami, H. (1998). Sapphirine-bearing granulites and related high-temperature metamorphic rocks from the Higo metamorphic terrane, west-central Kyushu. *Journal of Metamorphic Geology* **16**, 53–66.

Pattison, D. R., Chacko, T., Farquhar, J. & Mcfarlane, C. R. (2003). Temperatures of granulite-facies metamorphism: constraints from experimental phase equilibria and thermobarometry corrected for retrograde exchange. *Journal of Petrology* **44**, 867–900.

Peng, P., Guo, J. H., Zhai, M. G. & Bleeker, W. (2010). Paleoproterozoic gabbronoritic and granitic magmatism in the northern margin of the North China Craton: evidence of crust–mantle interaction. *Precambrian Research* **183**, 635–659.

Pilugin, S. M., Fonarev, V. I. & Savko, K. A. (2009). Feldspar thermometry of ultrahigh-temperature (>1000 °C) metapelites from the Voronezh Crystalline Massif (Kurske-Besedino Granulite Block). *Doklady Earth Sciences* **425**, 201–204.

Platt, J. P., Soto, J. I., Whitehouse, M. J., Hurford, A. J. & Kelley, S. P. (1998). Thermal evolution, rate of exhumation, and tectonic significance of metamorphic rocks from the floor of the Alboran extensional basin. *Tectonics* **17**, 671–689.

Powell, R. & Holland, T. J. B. (1988). An internally consistent thermodynamic dataset with uncertainities and correlations. 3. Application, methods, and worked examples and a computer program. *Journal of Metamorphic Geology* **6**, 173–204.

Powell, R. & Holland, T. J. B. (1993). On the formulation of simple mixing models for complex phases. *American Mineralogist* **78**, 1174–1180.

Raith, M., Karmakar, S. & Brown, M. (1997). Ultra-high-temperature metamorphism and multistage decompressional evolution of sapphirine granulites from the Palni Hill Ranges, southern India. *Journal of Metamorphic Geology* **15**, 379–399.

Rao, C. V. D., Santosh, M. & Chmielowski, R. M. (2012). Sapphirine granulites from Panasapattu, Eastern Ghats belt, India: Ultrahigh-temperature metamorphism in a Proterozoic convergent plate margin. *Geoscience Frontiers* **3**, 9–31.

Roscoe, R. (1952). The viscosity of suspensions of rigid spheres. *British Journal of Applied Physics* **3**, 267–269.

Sajeev, K. & Osanai, Y. (2004). Ultrahigh-temperature metamorphism (1150 °C, 12 kbar) and multistage evolution of Mg-, Al-rich granulites from the central Highland complex, Sri Lanka. *Journal of Petrology* **45**, 1821–1844.

Santosh, M., Liu, D., Shi, Y. & Liu, S. J. (2013). Paleoproterozoic accretionary orogenesis in the North China Craton: a SHRIMP zircon study. *Precambrian Research* **227**, 29–54.

Santosh, M., Liu, S. J., Tsunogae, T. & Li, J. H. (2012). Paleoproterozoic ultrahigh-temperature granulites in the North China Craton: implications for tectonic models on extreme crustal metamorphism. *Precambrian Research* **222-223**, 77–106.

Santosh, M. & Omori, S. (2008). CO_2 windows from mantle to atmosphere: models on ultrahigh-temperature metamorphism and speculations on the link with melting of snowball earth. *Gondwana Research* **14**, 82–96.

Santosh, M., Sajeev, K., Li, J. H., Liu, S. J. & Itaya, T. (2009). Counterclockwise exhumation of a hot orogen: the Paleoproterozoic ultrahigh-temperature granulites in the North China Craton. *Lithos* **110**, 140–152.

Santosh, M., Tsunogae, T., Li, J. H. & Liu, S. J. (2007b). Discovery of sapphirine-bearing mg–al granulites in the North China Craton: implications for Paleoproterozoic ultrahigh temperature metamorphism. *Gondwana Research* **11**, 263–285.

Santosh, M., Tsunogae, T., Ohyama, H., Sato, K., Li, J. H. & Liu, S. J. (2008). Carbonic metamorphism at ultrahigh-temperatures: Evidence from North China Craton. *Earth and Planetary Science Letters* **266**, 149–165.

Santosh, M., Wilde, S. A. & Li, J. H. (2007a). Timing of Paleoproterozoic ultrahigh-temperature metamorphism in the north china craton: evidence from SHRIMP U-Pb zircon geochronology. *Precambrian Research* **159**, 178–196.

Sarkar, S., Dasgupta, S. & Fukuoka, M. (2003). Petrological evolution of a suite of spinel granulites from Vizianagram, Eastern Ghats belt, India, and genesis of sapphirine-bearing assemblages. *Journal of Metamorphic Geology* **21**, 899–913.

Sassi, R., Mazzoli, C., Spiess, R. & Cester, T. (2004). Towards a better understanding of the fibrolite problem: the effect of reaction overstepping and surface energy anisotropy. *Journal of Petrology* **45**, 1467–1479.

Sauerzapf, U., Lattard, D., Burchard, M. & Engelmann, R. (2008). The titanomagnetite–ilmenite equilibrium: new experimental data and thermo-oxybarometric application to the crystallization of basic to intermediate rocks. *Journal of Petrology* **49**, 1161–1185.

Schreyer, W., Bernhardt, H., Fransolet, A. & Armbruster, T. (2004). End-member ferrian kanonaite: an andalusite phase with one Al fully replaced by $(Mn, Fe)^{3+}$ in a quartz vein from the Ardennes mountains, Belgium, and its origin. *Contributions to Mineralogy and Petrology* **147**, 276–287.

Sengupta, P., Karmakar, S., Dasgupta, S. & Fukuoka, M. (1991). Petrology of spinel granulites from Araku, Eastern Ghats, India, and a petrogenetic grid for sapphirine-free rocks in the system FMAS. *Journal of Metamorphic Geology* **9**, 451–459.

Shaw, H. R. (1972). Viscosity of magmatic silicate liquids: an empirical method of prediction. *American Journal of Science* **272**, 870–893.

Shi, Q., Dong, X. J., Xu, Z. Y., Guan, Q. B., Li, P. C., Zhang, C. & Cui, F. H. (2018). Anatectic origin and geological significance of the Paleoproterozoic gneissic garnet granite in the Jining area, northern margin of the North China Craton. *Acta Petrologica Sinica* **34**, 2754–2772 (in Chinese with English abstract).

Shimizu, H., Tsunogae, T., Santosh, M., Liu, S. J. & Li, J. H. (2013). Phase equilibrium modelling of Palaeoproterozoic ultrahigh-temperature sapphirine granulite from the Inner Mongolia Suture Zone, North China Craton: implications for counterclockwise P-T path. *Geological Journal* **48**, 456–466.

Sizova, E., Gerya, T. & Brown, M. (2014). Contrasting styles of Phanerozoic and Precambrian continental collision. *Gondwana Research* **25**, 522–545.

Stevens, G., Clemens, J. D. & Droop, G. T. R. (1997). Melt production during granulite facies anatexis: experimental data

from "primitive" metasedimentary protoliths. *Contributions to Mineralogy and Petrology* **128**, 352–370.

Tucker, N. M., Hand, M. & Payne, J. L. (2015). A rift-related origin for regional mediumpressure, high-temperature metamorphism. *Earth and Planetary Science Letters* **421**, 75–88.

Wan, Y., Song, B., Liu, D., Wilde, S. A., Wu, J., Shi, Y., Yin, X. & Zhou, H. (2006). SHRIMP U-Pb zircon geochronology of Palaeoproterozoic metasedimentary rocks in the North China Craton: evidence for a major Late Palaeoproterozoic tectonothermal event. *Precambrian Research* **149**, 249–271.

Wan, Y., Xu, Z., Dong, C., Nutman, A., Ma, M., Xie, H., Liu, S., Liu, D., Wang, H. & Cu, H. (2013). Episodic Paleoproterozoic (∼ 2.45, ∼1.95 and ∼1.85 Ga) mafic magmatism and associated high temperature metamorphism in the Daqingshan area, North China Craton: SHRIMP zircon U-Pb dating and whole-rock geochemistry. *Precambrian Research* **224**, 71–93.

Wan, Y. S., Liu, D. Y., Dong, C. Y., Xu, Z. Y., Wang, Z. J., Wilde, S. A. & Zhou, H. Y. (2009). The Precambrian Khondalite Belt in the Daqingshan Area, North China Craton: Evidence for Multiple Metamorphic Events in the Palaeoproterozoic Era. In: Reddy, S. M., Mazumder, R., Evans, D. A. D. & Collins, A. S. (eds) *Palaeoproterozoic Supercontinents and Global Evolution*. London: Geological Society London, Special Publication **323**, pp. 73–97.

Wang, B., Tian, W., Wei, C. J. & Di, Y. K. (2019). Ultrahigh metamorphic temperatures over 1050 °C recorded by Fe-Ti oxides and implications for Paleoproterozoic magma-induced crustal thermal perturbation in Jining area, North China Craton. *Lithos* **348-349**, 105180.

Wang, L. J., Guo, J. H., Yin, C. Q., Peng, P., Zhang, J., Spencer, C. J. & Qian, J. H. (2018). High-temperature S-type granitoids (charnockites) in the Jining complex, North China Craton: Restite entrainment and hybridization with mafic magma. *Lithos* **320-321**, 435–453.

Wei, C. J., Powell, R. & Clarke, G. L. (2004). Calculated phase equilibria for low- and medium-pressure metapelites in the KFMASH and KMnFMAS systems. *Journal of Metamorphic Geology* **22**, 495–508.

Wei, C. J., Qian, J. H. & Zhou, X. W. (2014). Paleoproterozoic crustal evolution of the Hengshan-Wutai-Fuping region. *Geoscience Frontiers* **5**, 485–497.

Wheller, C. J. & Powell, R. (2014). A new thermodynamic model for sapphirine: calculated phase equilibria in $K_2O–FeO–MgO–Al_2O_3–SiO_2–H_2O–TiO_2–Fe_2O_3$. *Journal of Metamorphic Geology* **32**, 287–299.

White, R. W., Powell, R., Holland, T. J. B., Johnson, T. E. & Green, E. C. R. (2014a). New mineral activity–composition relations for thermodynamic calculations in metapelitic systems. *Journal of Metamorphic Geology* **32**, 261–286.

White, R. W., Powell, R. & Johnson, T. E. (2014b). The effect of Mn on mineral stability in metapelites revisited: new a-x relations for manganese-bearing minerals. *Journal of Metamorphic Geology* **32**, 809–828.

Williams, I. S. (1998). U–Th–Pb geochronology by ion microprobe. In: McKibben, M. A., Shanks, W. C. & Ridely, W. I. (eds) *Applications of Microanalytical Techniques to Understanding Mineralizing Processes. Reviews in Economic Geology*. Toronto: The Society, pp. 1–35.

Wu, C. H., Sun, M., Li, H., Zhao, G. & Xia, X. (2006). LA-ICP-MS U-Pb zircon ages of the khondalites from the Wulashan and Jining high-grade terrain in northern margin of the North China Craton: Constraints on sedimentary age of the khondalite. *Acta Petrologica Sinica* **22**, 2639–2654 (in Chinese with English abstract).

Yang, Q. Y., Santosh, M. & Tsunogae, T. (2014). Ultrahigh temperature metamorphism under isobaric heating: new

evidence from the North China Craton. *Journal of Asian Earth Sciences* **95**, 2–16.

Yin, C. Q., Zhao, G. C., Guo, J. H., Sun, M., Xia, X., Zhou, X. & Liu, C. (2011). U-Pb and Hf isotopic study of zircons of the Helanshan Complex: constrains on the evolution of the Khondalite Belt in the Western Block of the North China Craton. *Lithos* **122**, 25–38.

Yin, C. Q., Zhao, G. C., Sun, M., Xia, X. P., Wei, C. J., Zhou, X. W. & Leung, W. (2009). LA-ICP-MS U-Pb zircon ages of the Qianlishan Complex: constrains on the evolution of the Khondalite Belt in the Western Block of the North China Craton. *Precambrian Research* **174**, 78–94.

Zhai, M. G. & Peng, P. (2007). Paleoproterozoic events in the North China craton. *Acta Petrologica Sinica* **23**, 2665–2682 (in Chinese with English abstract).

Zhang, H. T., Li, J. H., Liu, S. J., Li, W. S., Santosh, M. & Wang, H. H. (2012). Spinel + quartz-bearing ultrahigh-temperature granulites from Xumayao, Inner Mongolia Suture Zone, North China Craton: petrology, phase equilibria and counterclockwise p–T path. *Geoscience Frontiers* **3**, 603–611.

Zhang, Z. M., Xiang, H., Dong, X., Ding, H. X. & He, Z. Y. (2015). Long-lived high-temperature granulite-facies metamorphism in the Eastern Himalayan orogen, south Tibet. *Lithos* **212-215**, 1–15.

Zhao, G., Cawood, P. A., Li, S., Wilde, S. A., Sun, M., Zhang, J., He, Y. & Yin, C. (2012). Amalgamation of the North China Craton: Key issues and discussion. *Precambrian Research* **222-223**, 55–76.

Zhao, G. C. (2009). Metamorphic evolution of major tectonic units in the basement of the North China Craton: Key issues and discussion. *Acta Petrologica Sinica* **25**, 1772–1792 (in Chinese with English abstract).

Zhao, G. C., Sun, M., Wilde, S. A. & Li, S. Z. (2005). Late Archean to Paleoproterozoic evolution of the North China Craton: Key issues revisited. *Precambrian Research* **136**, 177–202.

Zhao, G. C., Wilde, S. A., Cawood, P. A. & Lu, L. Z. (1999). Tectonothermal history of the basement rocks in the western zone of the North China Craton and its tectonic implications. *Tectonophysics* **310**, 37–53.

Zheng, Y. F. & Chen, R. X. (2017). Regional metamorphism at extreme conditions: Implications for orogeny at convergent plate margins. *Journal of Asian Earth Sciences* **145**, 46–73.

Zhong, C. T., Deng, J. F. & Wan, Y. S. (2007). Magma recording of Paleoproterozoic orogeny in central segment of northern margin of North China Craton: geochemical characteristics and zircon shrimp dating of s-type granitoids. *Geochimica* **36**, 585–600.

Zhou, X. W., Zhao, G. C. & Geng, Y. S. (2010). Helanshan high pressure pelitic granulite: petrologic evidence for collision event in the western block of the North China Craton. *Acta Petrologica Sinica* **26**, 2113–2121 (in Chinese with English abstract).

APPENDIX

The stoichiometric formula of ferric-sillimanite is coded as $(Fe_xAl_{1-x})AlSiO_5$ with x ranging from 0–1, which involves $Fe^{3+}–Al^{VI}$ substitution on the octahedral site (e.g. Grambling & Williams, 1985; Schreyer *et al.*, 2004). It is a solid solution between Al_2SiO_5 (sill) and $FeAlSiO_5$ (fsill) in symmetric formalism (SF; Powell & Holland, 1993). The SF interaction energy adopted is $W_{(sill, fsill)} =$ 1 kJ calculated by $W–w$ relations (Powell & Holland, 1993), $W_{(sill, fsill)} = w$oct (Al, Fe^{3+}) = 1 kJ, where $w$oct

(Al, Fe^{3+}) is obtained from $W_{(cz,\ ep)}$, $W_{(mgts,\ fopx)}$, $W_{(east,\ fbi)}$ and $W_{(spr5,\ ospr)}$ in previously coded minerals (ep, opx, bi and sa; Holland & Powell, 2011; White *et al.*, 2014*a*; Wheller & Powell, 2014). The Gibbs energy of end-member $FeAlSiO_5$ is made with $G_{fsill} = G_{sill} + \frac{1}{2} G_{andr} - \frac{1}{2} G_{gr} + \Delta H_{fsill}$, where ΔH_{fsill} refers DQF in THERMOCALC (White *et al.*, 2014*a*) and equals to $\Delta_f H_{fsill} - (\Delta_f H_{sill} + \frac{1}{2}\Delta_f H_{andr} - \frac{1}{2}\Delta_f H_{gr})$ following Hess's law. The enthalpy of formation $\Delta_f H_{fsill}$ approximates the $\Delta_f H$ sum of the most stable oxides of relevant elements ($\Delta_f H_{fsill} \approx \Delta_f H_q + \frac{1}{2}\Delta_f H_{cor} + \frac{1}{3}\Delta_f H_{mt}$). Based on the thermodynamic dataset of Holland & Powell (2011), the parameter is estimated to be DQF $= \Delta H_{fsill} = 29.06$ kJ/mol, which corresponds to the experimentally constrained ΔH of ferric-corundum (29.0 ± 2.5 kJ/mol; Majzlan *et al.*, 2002) due to the negligible enthalpy change on the combination of quartz and corundum (~ 0.5 kJ; Charlu *et al.*, 1975).